Please cite this article in press as: Guo et al., Single-Cell RNA Sequencing of Human Embryonic Stem Cell Differentiation Delineates Adverse Effects of Nicotine on Embryonic Development, Stem Cell Reports (2019), https://doi.org/10.1016/j.stemcr.2019.01.022

Stem Cell Reports
Article

OPEN ACCESS

# Single-Cell RNA Sequencing of Human Embryonic Stem Cell Differentiation Delineates Adverse Effects of Nicotine on Embryonic Development

Hongchao Guo,[1,2,3,5] Lei Tian,[1,2,3,5] Joe Z. Zhang,[1,2,3] Tomoya Kitani,[1,2,3] David T. Paik,[1,2,3] Won Hee Lee,[4] and Joseph C. Wu[1,2,3,*]

[1]Stanford Cardiovascular Institute, 265 Campus Drive G1120B, Stanford, CA 94305, USA
[2]Institute for Stem Cell Biology and Regenerative Medicine, Stanford, CA 94305, USA
[3]Division of Cardiology, Department of Medicine, Stanford University School of Medicine, Stanford, CA 94305, USA
[4]Department of Basic Medical Sciences, University of Arizona College of Medicine, Phoenix, AZ 85004, USA
[5]Co-first author
*Correspondence: joewu@stanford.edu
https://doi.org/10.1016/j.stemcr.2019.01.022

## SUMMARY

Nicotine, the main chemical constituent of tobacco, is highly detrimental to the developing fetus by increasing the risk of gestational complications and organ disorders. The effects of nicotine on human embryonic development and related mechanisms, however, remain poorly understood. Here, we performed single-cell RNA sequencing (scRNA-seq) of human embryonic stem cell (hESC)-derived embryoid body (EB) in the presence or absence of nicotine. Nicotine-induced lineage-specific responses and dysregulated cell-to-cell communication in EBs, shedding light on the adverse effects of nicotine on human embryonic development. In addition, nicotine reduced cell viability, increased reactive oxygen species (ROS), and altered cell cycling in EBs. Abnormal $Ca^{2+}$ signaling was found in muscle cells upon nicotine exposure, as verified in hESC-derived cardiomyocytes. Consequently, our scRNA-seq data suggest direct adverse effects of nicotine on hESC differentiation at the single-cell level and offer a new method for evaluating drug and environmental toxicity on human embryonic development *in utero*.

## INTRODUCTION

Maternal smoking during pregnancy is an established risk factor for birth defects such as miscarriage, growth restriction, and premature birth (Jaddoe et al., 2008). It is closely associated with adverse neurobehavioral, cardiovascular, respiratory, endocrine, and metabolic outcomes in the offspring, which can persist into adulthood (Holbrook, 2016). Nicotine, the main chemical constituent of tobacco smoking, is primarily responsible for the elevated risk (Holbrook, 2016). Unfortunately, the introduction and spread of new tobacco products containing nicotine, such as e-cigarettes, is reversing recent progress toward reduction of tobacco use (Bao et al., 2018).

A large body of research has elucidated the negative effects of nicotine in animals, mainly in rodent models. Animal studies have demonstrated that nicotine exposure during pregnancy has detrimental effects on fetal development, such as cellular damage, increased inflammation (Mohsenzadeh et al., 2014), oxidative stress (Lin et al., 2014), endoplasmic reticulum stress (Wong et al., 2016), and impaired cell replication (Repo et al., 2014; Slotkin et al., 1987). The suitability of clinical translation of these studies, however, remains questionable due to interspecies physiological differences and uncertainty over the degree and route of nicotine exposure (Tizabi, 2007; Winzer-Serhan, 2008). To address these issues, some studies have attempted to study the effects of nicotine using human cells. For example, using microarray analysis, Liszewski et al. (2012) demonstrated that tobacco smoke and nicotine have lineage- and stage-specific effects on differentiated human embryonic stem cell (hESCs).

Although the *in vitro* differentiation of embryonic body (EB) model can be used to mimic early developments from pre-implantation epiblasts to lineage-committed progenitors, conventional bulk RNA sequencing (RNA-seq) analysis has limitations for studying the individual cellular heterogeneity within the EBs. With the recent advent of microdroplet-based single-cell RNA-seq (scRNA-seq) technologies, it is now feasible to analyze transcriptomes at the single-cell level within heterogeneous cell populations (Blakeley et al., 2017; Paik et al., 2018). Here, we used scRNA-seq of EBs to characterize the effects of nicotine on hESC differentiation. We found that nicotine exposure reduced cell viability and increased reactive oxygen species (ROS), resulting in aberrant formation and differentiation of EBs. Nicotine exposure also altered cell cycling in endothelial, stromal, and muscle progenitor cells differentiated from hESCs. Furthermore, nicotine caused lineage-specific effects and dysregulated cell-to-cell communication. We found abnormal $Ca^{2+}$ signaling pathways in muscle cells upon nicotine exposure that was verified using hESC-derived cardiomyocytes. Taken together, the effects of nicotine exposure on hESC differentiation at the single-cell transcriptomic level offer new insights into mechanisms of nicotine toxicity on early embryonic development, and can provide new tools for optimizing drug toxicity screening.

Please cite this article in press as: Guo et al., Single-Cell RNA Sequencing of Human Embryonic Stem Cell Differentiation Delineates Adverse Effects of Nicotine on Embryonic Development, Stem Cell Reports (2019), https://doi.org/10.1016/j.stemcr.2019.01.022

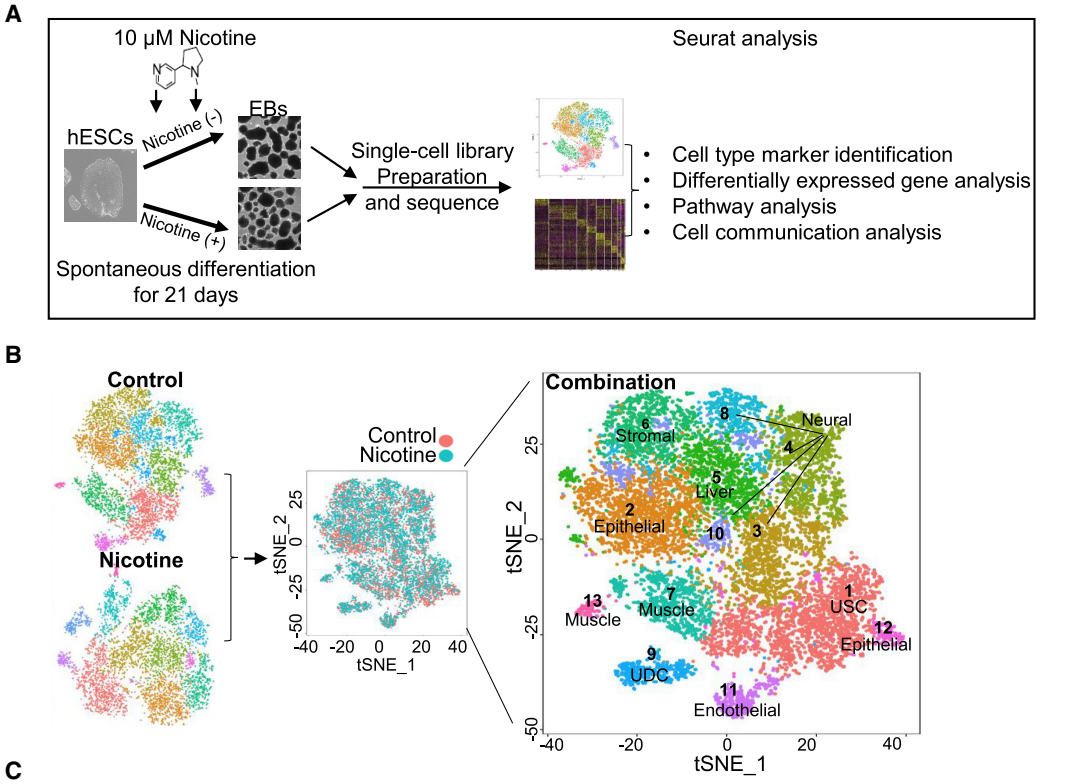


(legend on next page)

Please cite this article in press as: Guo et al., Single-Cell RNA Sequencing of Human Embryonic Stem Cell Differentiation Delineates Adverse Effects of Nicotine on Embryonic Development, Stem Cell Reports (2019), https://doi.org/10.1016/j.stemcr.2019.01.022

## RESULTS

### scRNA-Seq Analysis Reveals Six Major Types of Progenitor Cells

To investigate the effects of nicotine on hESC differentiation, we performed microdroplet-based scRNA-seq to identify unique cell lineages on day 21 control and nicotine-exposed EBs (Figure 1A). We used 10 μM nicotine exposure for 21 days, which is similar to nicotine concentrations found in fetal serum (Luck et al., 1985) and has been used in prior hESC studies (Hirata et al., 2016; Zdravkovic et al., 2008). After dissociation, transcriptomic data of 5,646 single cells from nicotine-exposed EBs and 6,847 single cells from control EBs were acquired. Sequenced data showed high read depth, and were mapped to approximately 3,000 median genes per cell (Figure S1A, left). The percentage of mitochondrial genes present in most cells was less than 10% (Figure S1A, right). We used the Seurat package (Satija et al., 2015) to perform principal-component analysis and t-distributed stochastic neighbor embedding (t-SNE) analysis. Control EBs were divided into 13 clusters, and nicotine-exposed EBs were divided into 12 clusters that exhibited distinct gene expression patterns (Figures S1B and S1C). Control and nicotine-exposed EBs contained similar cell-type markers, without any observed differences in cell types between the two samples (Figure S1B).

Next, we performed integrative analysis to compare the cell proportions and gene expression differences in each cell type between nicotine and control EBs. Nicotine exposure induced widespread transcriptomic changes, which were manifested as a shift in the t-SNE projections of singlets (Figure 1B, middle). Previous reports with bulk RNA-seq data also indicated that nicotine affects gene expression in multiple cell lineages (Liszewski et al., 2012). A total of 13 individual clusters were defined from the combined datasets (termed C1 to C13) (Figure 1B, right). Based on differential genes enriched in each cluster, six major types of progenitor cells were identified by Seurat (Figures 1C and 1D). Clusters 3, 4, 8, and 10 were associated with high expression of *LHX2* and *NR2F1* (de Melo et al., 2016; Tang et al., 2010) and annotated as neural cells. Cluster 5 represented liver progenitor cells with a high expression of *FRZB* and *PTN* (Michelotti et al., 2014; Shen et al., 2015). Cluster 6 was annotated as stromal progenitor cells with a high expression of *SFRP2* and *COL2A1* (Saito et al., 2013; Tabib et al., 2018). Cluster 11 was annotated as endothelial progenitor cells with high expression of *GDF15* and *DDIT3* (Ahrens et al., 2011; Loinard et al., 2012). Cluster 2 and 12 were annotated as epithelial progenitor cells (EpiPCs) with high expression of *IGFBP5* and *PODXL* (Sugrue et al., 2016; Zhu et al., 2016). Clusters 7 and 13 showed a high expression of *HAPLN1* and *S100A11*, and were annotated as muscle progenitor cells (DeLaughter et al., 2013; Malmstrom et al., 2004). Cluster 1 was enriched for pluripotency genes such as *TERF1* and *POU5F1*, and was annotated as "undifferentiated stem-like cells". Cluster 9 was enriched for cytoskeletal genes such as *ACTB* and *TUBB*, and was annotated as "undetermined cells".

To further confirm our cluster annotation, we found genes specifically expressed in each cell type that were enriched for the expected appropriate gene ontology (GO) terms. For example, genes that were specifically expressed in muscle progenitor cell clusters were significantly enriched for the cytosolic $Ca^{2+}$ pathway ($p = 2.92 \times 10^{-11}$) and skeletal system development ($p = 3.36 \times 10^{-4}$). Genes expression in the neural progenitor cell clusters were significantly enriched for nervous system development ($p = 1.01 \times 10^{-6}$) and sensory organ development ($p = 5.60 \times 10^{-8}$). Genes expression in the liver progenitor cell cluster were enriched for liver development ($p = 2.52 \times 10^{-4}$) and response to lipid ($p = 1.74 \times 10^{-2}$). Genes expression in the endothelial progenitor cell cluster were significantly enriched for blood vessel development ($p = 1.3 \times 10^{-4}$) and angiogenesis ($p = 1.61 \times 10^{-3}$). Genes expressions in the EpiPC clusters were enriched for lung development ($p = 2.43 \times 10^{-5}$) and kidney development ($p = 5.67 \times 10^{-4}$) (Figure S1D).

**Figure 1. scRNA-Seq Analysis Reveals Cell Lineages in Control and Nicotine-Exposed Embryoid Bodies**

(A) Process flow diagram of scRNA-seq analysis on hESC differentiation. Single cells were collected from two independent EB differentiation experiments from day 21 EBs (nicotine-exposed versus control) and were prepared by single-cell barcoded droplets and chemicals from 10× Genomics. Bioinformatics data were processed using Seurat. Cell-type marker, differentially expressed gene, cell communication, and pathway analyses were performed to investigate the effects of nicotine exposure on hESC differentiation.

(B) Separated (left) and combined (middle and right) t-SNE plots of single cells from control and nicotine-exposed EBs. We defined six main types of progenitor cells in day 21 EBs, including muscle progenitor cells (clusters 3 and 13), liver progenitor cells (cluster 5), neural progenitor cells (clusters 3, 4, 8, and 11), stromal progenitor cells (cluster 6), epithelial progenitor cells (clusters 2 and 12), and endothelial progenitor cells (cluster 11). In addition, undifferentiated stem-like cells (USCs) (cluster 1) and undetermined cells (UDCs) (cluster 9) were also identified.

(C) Heatmap showing the expression pattern of top 10 differential genes in each cell type. Representative differential genes for each cell type are listed on the right side. The complete lists of differential genes for each cell type are listed in Table S3.

(D) Violin plots show the expression level distributions of marker genes across cell types.

Please cite this article in press as: Guo et al., Single-Cell RNA Sequencing of Human Embryonic Stem Cell Differentiation Delineates Adverse Effects of Nicotine on Embryonic Development, Stem Cell Reports (2019), https://doi.org/10.1016/j.stemcr.2019.01.022

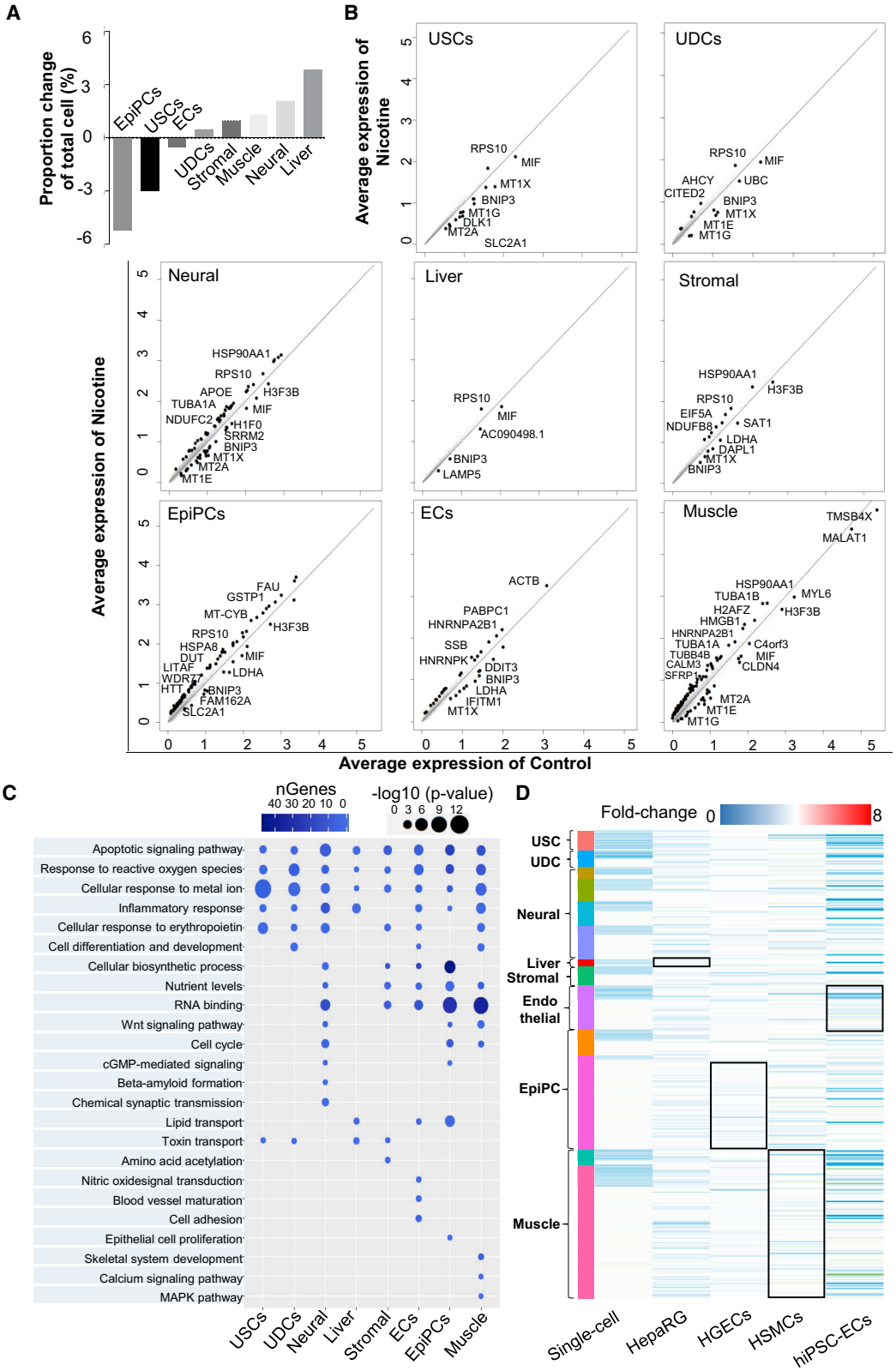


*(legend on next page)*

It should be noted that neural, muscle, and epithelial progenitor cells consisted of several sub-clusters. Neural progenitor cells were further divided into four subsets: clusters 3, 4, 8, and 10. Cluster 3 showed a high expression of *LHX5/HESX1* that is related to forebrain development (Martynova et al., 2018; Zhao et al., 1999). Cluster 4 was enriched for *HMGB2* and *PTTG1*, which are highly expressed in proliferating neural stem cells (Kimura et al., 2018). Cluster 8 was annotated as neural progenitor cells with an enrichment of *HNRNPH1* and *PTPRS* (Tchetchelnitski et al., 2014; Yazdani et al., 2015), which are related to sensory neurons development. Cluster 10 was enriched for *LHX2* and *NR2F1* and expressed eye development genes (de Melo et al., 2016; Tang et al., 2010). Muscle progenitor cells were divided into two subsets: clusters 7 and 13. Cluster 7 was annotated as muscle cells for the expression of *HAPLN1* and *S100A11*, which are highly expressed in smooth muscle cells (DeLaughter et al., 2013; Malmstrom et al., 2004). Cluster 13 was enriched for *ZFHX3* and *NR2F2*, which are related to cardiac muscle development (Berry et al., 2001; Pei et al., 2017). EpiPCs were divided into two subsets: clusters 2 and 12. Cluster 2 was enriched for *IGFBP5* and *HES1*, which are related to eye development (Liu et al., 2013; Sugrue et al., 2016). Cluster 12 was enriched for *B3GNT7* and *PODXL*, which are highly expressed in stem-like epithelial cells (Dumont-Lagace et al., 2017) (Figures 1D and S1D).

Overall, six major types of progenitors (neural, liver, stromal, endothelial, epithelial, and muscle) were identified from scRNA-seq data of EBs based on cell markers detected by Seurat. These data may be useful for modeling nicotine exposure on individual organs and cells within the developing fetus.

## Nicotine Elicits Cell-Type-Specific Response in Differentiated EBs

Integrated analysis of control and nicotine-exposed EBs at the single-cell level enables us to quantitatively assess cell-type-specific responses to nicotine. Quantification of the cell-type compositional changes showed changes from 5% reduction in epithelial progentior cells to 4% increase in liver progenitor cells following nicotine exposure (Figures 2A and S2A). Next, we performed comparative analysis and calculated the average expression of both the nicotine-exposed and control cells to determine differentially expressed genes (DEGs) in each cell type (Figure 2B). Interestingly, there was a marked difference in the number of DEGs among different cell types, ranging from 5 to 103 genes with a *p*-value less than 0.01 and a log fold-change more than 0.25. For example, we observed 5 DEGs in liver progenitor cells with nicotine treatment, whereas muscle progenitor cells exhibited the greatest number of 103 DEGs. Among these DEGs, *BNIP3*, and metallothionein family genes (*MT1X*, *MT1G*, *MT1E*, and *MT2A*) were uniformly downregulated and *RPS10* was upregualted in most of cell types (Figure 2B). *BNIP3* gene is an important regulator during long-term nicotine-induced cell death in several cell types (Erkan et al., 2005; Tang et al., 2007). Metallothionein family genes play a role in the protection against metal toxicity and oxidative stress, and have been shown to be suppressed in chronic smokers (Billatos et al., 2018). These genes are involved in apoptosis, ROS generation, mitochondrial function, and response to metal ion pathways (Figure 2C), indicating that EBs have poor cell survival upon nicotine exposure.

Nicotine also showed cell-type-specific responses. *APOE*, *TUBA1A*, and *NDUFC2* were significantly upregulated, and *H1F0* and *SRRM2* were downregulated, in neural progenitor cells (Figures 2B and 2C). Abnormal expression of these genes can lead to β-amyloid formation and increased synaptic transmission (Moreno-Gonzalez et al., 2013), brain malformations (Aiken et al., 2017), and intellectual disability (Tanaka et al., 2018). In muscle progenitor cells, the most upregulated gene following nicotine exposure was *HSP90AA1*, a myosin chaperone protein gene involved

**Figure 2. Nicotine Exposure Induces Cell-Type-Specific Response**

(A) Cell proportion fluctuation for each cell type with nicotine exposure. Cell proportion fluctuation for each cluster with nicotine exposure is shown in Figure S2A. USCs, undifferentiated stem-like cells; UDCs, undetermined cells; EpiPCs, epithelial progenitor cells; ECs, endothelial progenitor cells.

(B) Plots of the average expression of genes from control and nicotine-exposed EBs for each cell type. Significant differentially expressed genes are labeled in the plots ($p < 0.05$). The complete list of differentially expressed genes upon nicotine exposure for each cluster is shown in Table S5.

(C) Pathway enrichment analysis of statistically significant gene ontologies following nicotine exposure. The size of the circle represents the significance of gene ontologies, and the darkness of color represents the number of genes involved in the gene ontologies. The complete lists of differentially expressed gene-related pathways upon nicotine exposure for each cluster are listed in Table S6.

(D) Heatmap for differentially expressed genes in scRNA-seq data, public hepatic cell line (HepaRG), human gingival epithelium cell line (HGEC), human smooth muscle cells (HSMCs), and human iPSC-derived endothelial cell (hiPSC-ECs) in terms of fold-change (nicotine-exposed relative to control EBs). Each row represents a single differentially expressed gene identified in (B). The names of cell types are labeled on the left side. Differentially expressed genes in scRNA-seq data corresponding to the public datasets are labeled with a rectangle. See also Figure S2.

in muscle development and disease (Armant et al., 2016; Etard et al., 2015). Increased expression of *HMGB1*, known to regulate cardiac excitation-contraction coupling by enhancing the sarcoplasmic reticulum $Ca^{2+}$ leakage through Toll-like receptor 4 (TLR4)-ROS signaling in cardiac muscle cells, was also observed (Figures 2B, 2C, and S2C).

In stromal progenitor cells, *LDHA* and *DAPL1*, known to regulate nutrient levels and amino acid acetylation, were downregulated upon nicotine exposure (Figures 2B and 2C). *BINP3*, related to lipid metabolism, was downregulated in liver cells (Glick et al., 2012). In epithelial progenitor cells, macrophage migration inhibitory factor (*MIF*), which is associated with chronic obstructive pulmonary disease in human, was downregulated (Sauler et al., 2015). *WDR77*, required for proliferation of lung and prostate epithelial cells during development and tumorigenesis (Sheng and Wang, 2016), was upregulated in epithelial progenitor cells in the presence of nicotine (Figures 2B and 2C). In endothelial progenitor cells, *LDHA*, *DDIT3*, and *IFITM1* were downregulated, and *HNRNP2B1* was upregulated upon nicotine exposure (Figures 2B and 2C). Downregulation of *LDHA* is related to the suppression of glycolysis and endothelial cell dysfunction (Xu et al., 2016). Downregulated *DDIT3* exhibits reduced ER stress response upon long-term cigarette smoke exposure (Geraghty et al., 2011). *IFITM1* downregulation is related to endothelial lumen formation during angiogenesis (Popson et al., 2014) (Figures 2B and 2C). Likewise, we confirmed cell-type-specific responses to long-term nicotine exposure on EBs using GO pathway enrichment analysis (Figure 2C).

To determine how our analysis correlates with previously reported bulk RNA-seq data from specific cell lines, we examined the expression fold-changes of DEGs in published gene expression data after nicotine exposure, including hepatic cells (HepaRG), human gingival epithelium cells (HGECs), human smooth muscle cells (HSMCs), and human iPSC-derived endothelial cells (hiPSC-ECs) (De Abrew et al., 2016; Gumus et al., 2008; Yoshiyama et al., 2014). Interestingly, the trend in gene expression changes in cluster12 epithelial progenitor cell was similar to that of HGECs, whereas an opposite trend of gene expression changes was observed between cluster-2 epithelial progenitor cells and HGECs. This may be due to HGECs being more similar to stem-like "cluster-12 epithelial cell" in biological identity and more different from "cluster-2 epithelial cell". In HSMCs, the overall change of DEGs was subtle, but the trends in fold-change expression were consistent with EB-derived muscle cells. The genes downregulated in EB-derived endothelial cells also reduced their expression in hiPSC-ECs upon nicotine exposure (Figure 2D). Taken together, DEG analysis showed cell-type-specific transcriptomic changes upon nicotine exposure, which are consistent with previously reported bulk RNA-seq or microarray analysis in different cell types (De Abrew et al., 2016; Gumus et al., 2008; Yoshiyama et al., 2014). Our data thus provide a novel method for evaluating nicotine toxicity in heterogeneous populations of human EBs at a single-cell level.

## Nicotine Dysregulates Viability, ROS Generation, and Cell Cycle in EBs

Infants exposed to nicotine prenatally often exhibit lower birth weights than their peers (Fried and Oconnell, 1987; Slotkin, 1998). Animal studies have shown that nicotine exposure during pregnancy induces cellular damage, oxidative stress, and impaired cell replication (Repo et al., 2014; Slotkin et al., 1987). However, the molecular mechanisms remain poorly understood. Our DEG analysis showed that long-term nicotine exposure induced apoptosis and ROS generation mediated by the downregulation of *BNIP3* and metallothionein family genes (Figures 2B and 2C). Therefore, we performed several assays to confirm decreased survival of nicotine-exposed EB. Nicotine-exposed EBs were smaller than control EBs (Figures 3A and 3B), and cell viability was significantly reduced based on quantification of ATP, an indicator of metabolically active cells (Figure 3C). We also found higher levels of ROS in nicotine-exposed EBs compared with control EBs (Figure 3D).

Clinical and animal studies have shown that nicotine exposure changes the dynamics of cell replication and causes growth restriction (Repo et al., 2014). We thus analyzed cell cycling in the scRNA-seq data to evaluate the growth of EB after nicotine treatment by calculating cell-cycle phase scores based on canonical markers (Nestorowa et al., 2016). Relative to control EBs, nicotine-exposed EBs exhibited a 12% decrease in G1 phase, a 6% increase in G2M phase, and a 5.5% increase of S phase in endothelial progenitor cells. In stromal progenitor cells, we found an 11% decrease in G1 phase and a 12% increase in S phase (Figure S2B). Surprisingly, we found that there was a 20% decrease of cells in the G1 phase, a 5% increase of cells in the G2M phase, and a 15% increase of cells in S phase in the "cluster-13 muscle progenitor cell" (Figure 3E). For example, *TUBB4B*, a G2M phase marker, was differentially expressed in muscle progenitor cells from nicotine-exposed EBs versus control EBs (Figure 3F). Consequently, nicotine exposure increased ROS production and cell death in EBs and affected the cell cycle of endothelial, stromal, and muscle progenitor cells.

## Nicotine Exposure Dysregulates Cell-to-Cell Communication of Differentiated EBs

Smoking and nicotine consumption increase the pathological risk in endocrine, reproductive, respiratory, cardiovascular, and neurologic systems that all rely on intricate and dynamic interactions among multiple functional cell types for homeostasis and function (Kawasaki et al., 2011; Rehan et al., 2009). The effect of nicotine on

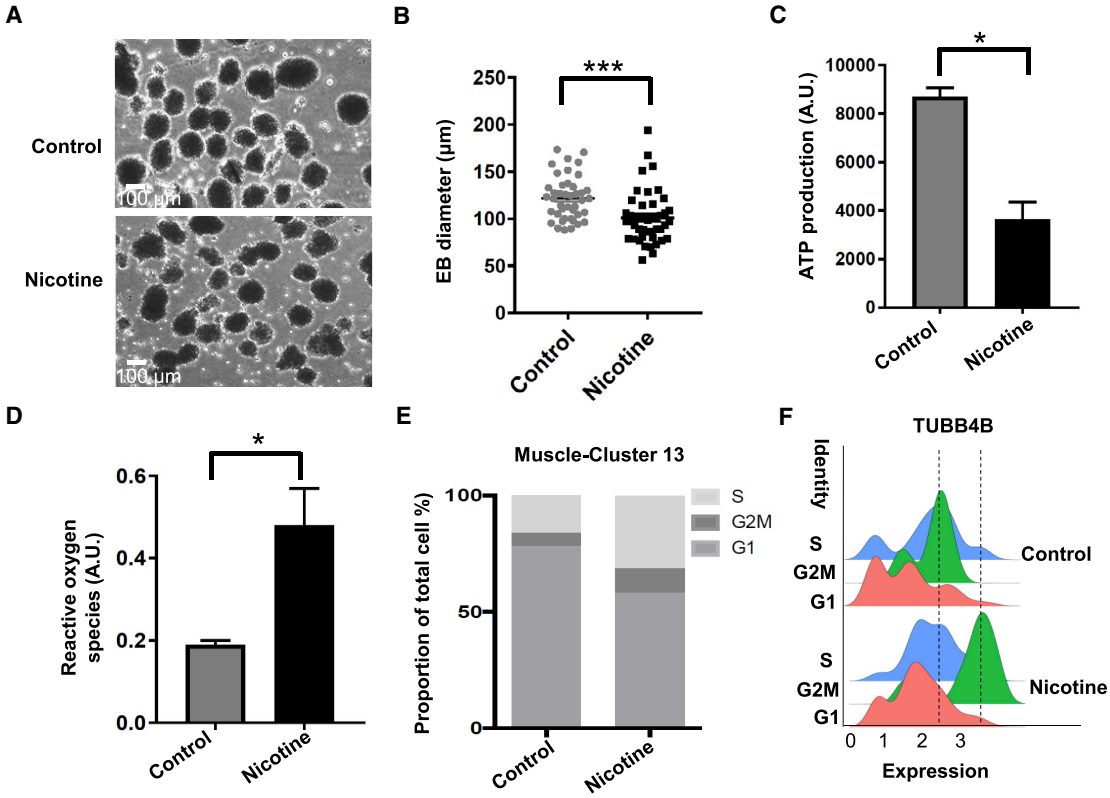


**Figure 3. Nicotine Reduces Cell Viability, Increases ROS Levels, and Changes Cell Cycle in EBs**

(A) Representative bright-field images of day 21 control and nicotine-exposed EBs. Scale bar, 100 μm.

(B) Size measurement of control (n = 45) and nicotine-exposed (n = 43) EBs in terms of diameter. EBs were collected from three independent EB differentiation experiments and pooled together for size measurement. ***$p < 0.001$.

(C) Cell viability assay of EBs based on quantitation of the ATP present in control and nicotine-exposed EBs. Cell viability were measured from three independent experiments. *$p < 0.05$.

(D) Reactive oxygen species (ROS) generation in control and nicotine-exposed EBs. ROS was measured from three independent experiments. *$p < 0.05$.

(E) Proportion of cluster 13 muscle cells in G2M, S, or G1 phase.

(F) Distribution of *TUBB4B* expression in three cell-cycle phases in control (top) and the nicotine-exposed EBs (bottom). Dashed lines represent the center of G2M phase in control and nicotine-exposed EBs.

cell-to-cell communication, however, is not well understood. Recent studies using *in vitro* co-cultured systems indicate that cell-to-cell communication could be affected by nicotine exposure (Holownia et al., 2015; Larsen et al., 2016; Liu et al., 2017). Our study used a dataset of human ligand-receptor pairs (Ramilowski et al., 2015) to define intercellular communication networks. To examine the effects of nicotine on cell-to-cell communication, we also analyzed ligand-receptor expression differences in nicotine-exposed EBs and control EBs. Overall, we observed increased intercellular communication for each EB cell type upon nicotine exposure (Figures 4A and 4B). For example, the number of ligand-receptor pairs in autocrine circuits from muscle progenitor cell was increased from 51 to 85, and the number of ligand-receptor pairs in muscle-neuron crosstalk was increased from 47 to 71 (Figure 4B).

Next, we analyzed the expression of ligands in each cell type to identify 61 ligands that were expressed in both nicotine-exposed EBs and control EBs, of which 7 were differentially expressed. Seventy-five ligands were mainly expressed in nicotine-exposed EBs, of which 3 were enriched in certain cell types identified by DEG analysis (Figures 4C and 4D). One extracellular ligand, high-mobility group box 1 (*HMGB1*), was uniformly upregulated in multiple cell types of nicotine-exposed EBs, but was not presented in control EBs (Figures 4C and 4D). Previous research has shown that HMGB1 regulates $Ca^{2+}$ handling and cellular contractility by activating its receptor Toll-like receptor 4 (TLR4) in rat cardiomyocytes, which plays an important role in the pathogenesis of cardiac dysfunction in many diseases (Zhang et al., 2014). Here, we found that HMGB1-TLR4 signaling, although not specific, was

Please cite this article in press as: Guo et al., Single-Cell RNA Sequencing of Human Embryonic Stem Cell Differentiation Delineates Adverse Effects of Nicotine on Embryonic Development, Stem Cell Reports (2019), https://doi.org/10.1016/j.stemcr.2019.01.022

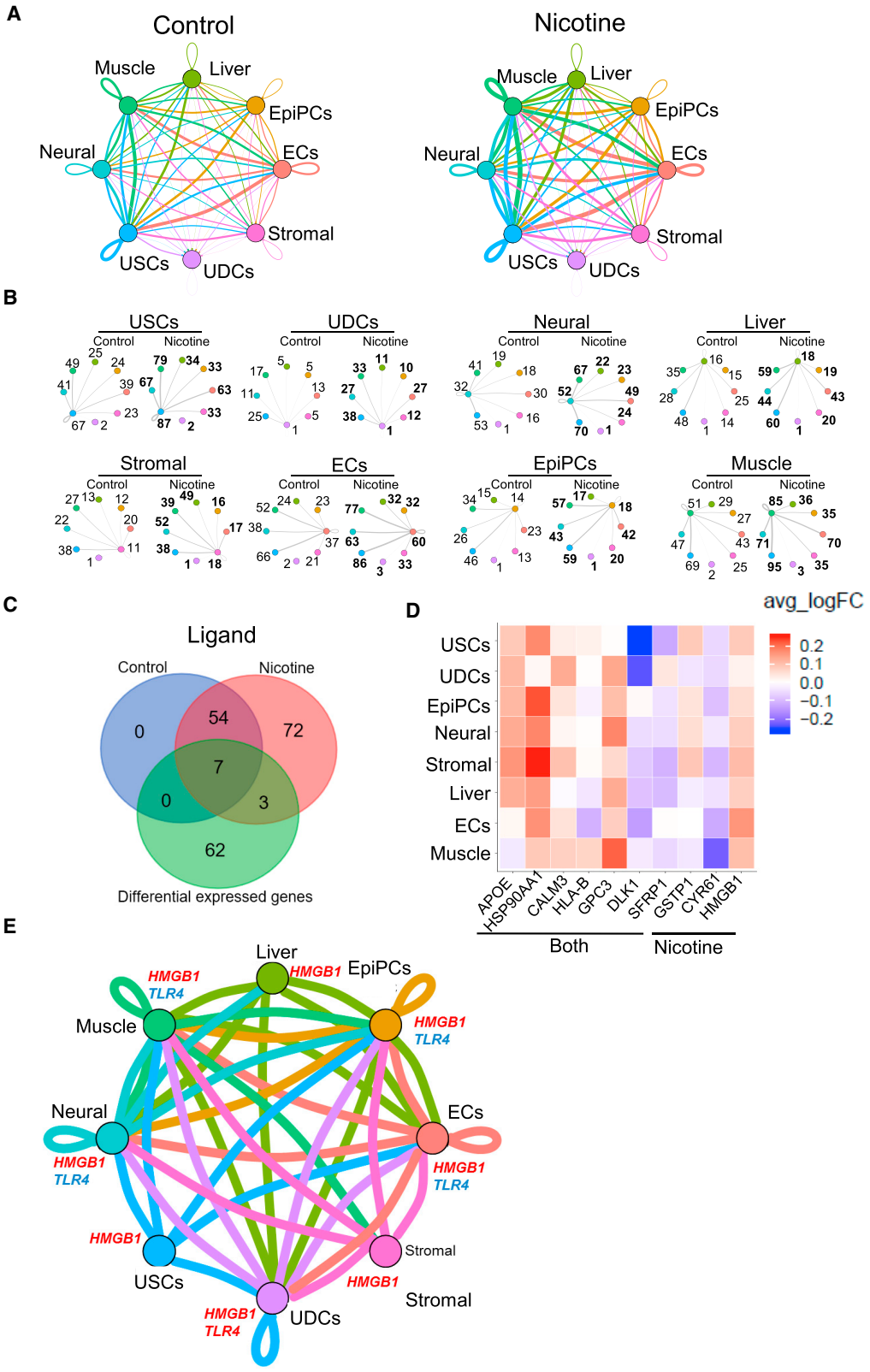


*(legend on next page)*

also activated in muscle progenitor cells (Figure 4E), suggesting that the activated HMGB1-TLR4 pathway may play an important role in cardiac dysfunction upon nicotine exposure.

### Disturbance of Intracellular $Ca^{2+}$ Handling in hESC-Derived Cardiomyocytes by Nicotine Exposure

Our data indicate that nicotine affects the expression of genes associated with intracellular $Ca^{2+}$ handling via the HMBG1-TLR4 pathway in cardiac muscle cells, and animal studies have shown that nicotine exposure disrupts intracellular $Ca^{2+}$ homeostasis in cardiac cells (Hu et al., 2013). To investigate whether nicotine affects the $Ca^{2+}$ handling in cardiac muscle cells, we first checked the expression of *HMGB1* and *TLR4* in hESC-derived cardiomyocytes. The expression of *HMGB1* was increased by 2-fold, and *TLR4* increased by 90-fold in hESC-derived cardiomyocytes exposed to nicotine (Figure 5A). We next conducted single-cell $Ca^{2+}$ measurement using Fura-2 in hESC-derived cardiomyocytes (Figure S3). As shown in Figures 5B–5E, nicotine increased the diastolic $Ca^{2+}$ (Figures 5B and 5C) and reduced the $Ca^{2+}$ transient amplitude (Figure 5D), accompanied by prolonged $Ca^{2+}$ decay (Figure 5E), suggesting compromised intracellular $Ca^{2+}$ homeostasis. We found that nicotine increased the propensity for arrhythmic $Ca^{2+}$ release in hESC-derived cardiomyocytes, as indicated by the arrows in Figures 5F and 5G. These data strongly suggest that nicotine increases $Ca^{2+}$-release abnormalities at the cellular level, predisposing these cells to $Ca^{2+}$-associated arrhythmia.

## DISCUSSION

In this study, we performed scRNA-seq analysis on a total of 12,500 single cells generated from human ESC-derived EBs following 21 days of culture with or without nicotine (Figure 1). Previous studies have demonstrated that nicotine concentrations in fetal serum are much higher than in maternal serum, ranging from 0.3 to 15.4 μM in fetal serum (Luck et al., 1985). Based on these reports, and the concentrations studied in other investigations of nicotine effect on hESCs (0.1–10.0 μM), we decided to use 10 μM of nicotine during hESC differentiation (Hirata et al., 2016; Zdravkovic et al., 2008). We also found that a 6-day exposure to nicotine reduces viability in hESCs (Figure S3D), suggesting that nicotine affects embryo development as early as the pre-implantation stage.

We did not observe cell-type differences between nicotine-exposed EBs and control EBs, although there were minor changes in the cell-type distribution upon nicotine exposure. However, DEG patterns from various progenitor cell populations indicated broad effects on cells derived from all three germ layers (neural, stromal, muscle, endothelial, and epithelial progenitor cells). This is consistent with clinical observations that nicotine-exposed infants have health problems throughout their lives, including impaired function of the endocrine, reproductive, respiratory, cardiovascular, and neurologic systems (Warren et al., 2014). In addition, although the current technology does not allow us to conduct proteomic analyses at a single-cell resolution level, we searched available nicotine-associated proteomic datasets in PubMed and found that our DEGs, HSPA8, BAX, and CKB were also reported to be upregulated in mouse neurons (Matsuura et al., 2016), MIF was downregulated in human endothelial cells (Zhang et al., 2014), and that SLC25A4, REEP5, and ATP5F1 were upregulated in human epithelial cells (Ghosh et al., 2018) (Figure S2E). Moreover, among these DEGs, *BNIP3* is uniformly downregulated in most cell types (Figure 2B). We observed downregulated BNIP3 expression in nicotine-exposed EBs compared with the control EBs at the protein level

**Figure 4. Nicotine Increased Cell-to-Cell Communication and Induced HMGB1-TLR4 Pathway among Cell Types in EBs**

(A) Intercellular communication analysis among cell types in the control and nicotine-exposed EBs. Line color indicates ligands broadcast by the cell population of the same color (labeled). Lines connect to cell populations where cognate receptors are expressed. Line thickness is proportional to the number of ligands where cognate receptors are present in the recipient cell population. Loops indicate autocrine circuits. Map quantifies potential communication but does not account for anatomic position or boundaries of cell populations. Crosstalk among cell types in control and nicotine-exposed EBs are listed in Table S7.

(B) Detailed view of ligands broadcast by each cell type and those populations expressing cognate receptors primed to receive a signal. Numbers indicate the quantity of ligand-receptor pairs for each inter-population link. Colors of the cell population corresponds to (A) above.

(C) Venn diagrams of ligands present in control or nicotine-exposed EBs and differentially expressed genes between control and nicotine-exposed EBs.

(D) Heatmap of the expression of differentially expressed ligands in control versus nicotine-exposed EBs across different cell types in terms of average fold-change of expression. Seven ligands present in both control and nicotine-exposed EBs (labeled "both") were selected as differentially expressed ligands. Three ligands were selected as expressed only in nicotine-exposed EBs and labeled as "nicotine."

(E) Intercellular communication analysis among different cell types shows activated HMGB1-TLR4 pathway upon nicotine exposure. The meaning of the thickness and color of line is explained in (A). USCs, undifferentiated stem-like cells; UDCs, undetermined cells; EpiPCs, epithelial progenitor cells; ECs, endothelial progenitor cells.

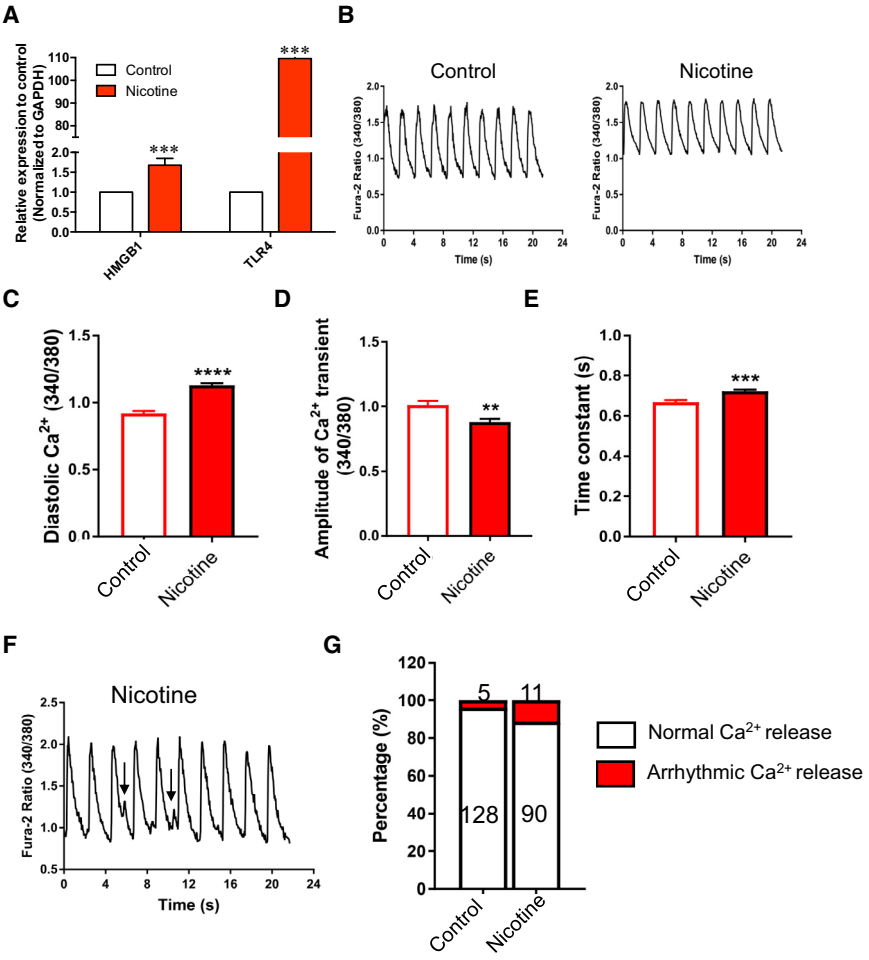


**Figure 5. Nicotine Disrupts Intracellular $Ca^{2+}$ Handling in hESC-Derived Cardiomyocytes**

(A) Real-time PCR verification of the expression levels of *HMGB1* and *TLR4* in hESC-derived cardiomyocytes for nicotine-exposed and control group. Real-time PCR was conducted from three independent differentiation experiments. Nicotine and ethanol were added during cardiomyocyte differentiation process. Ethanol-exposed hESC-derived cardiomyocytes were used as a control. ***$p < 0.001$.

(B–E) Representative single-cell $Ca^{2+}$ traces with and without treatment of nicotine (1 μM) (B). Cells were paced at 0.5 Hz and recorded at 37°C. Nicotine affects diastolic $Ca^{2+}$ (C), $Ca^{2+}$ transient amplitude (D), and $Ca^{2+}$ uptake (E).

(F) Representative arrhythmic $Ca^{2+}$ release. The arrhythmic $Ca^{2+}$ release is indicated by the arrows.

(G) Percentage of cells with normal or arrhythmic $Ca^{2+}$ release. Numbers indicate the recorded cell number in each condition. Recording was conducted with two independent differentiation. The cell number shows the pooled data.

**$p < 0.01$, ***$p < 0.001$. Error bars indicate SEM.

(Figure S2D). These lines of evidence suggest that our scRNA-seq data can reflect protein expression to some extent.

Our scRNA-seq analysis suggests that downregulation of *BNIP3* and metallothionein family gene expression in multiple progenitor cell types upon nicotine exposure provides the molecular mechanisms that lead to altered DEG patterns. It has been reported that reduced BNIP3 expression correlates with poor cell survival following long-term nicotine exposure (Tang et al., 2007). Our data indicate that hESC-derived cells adapt to long-term nicotine exposure and cell damage resulting from downregulation of *BNIP3* (Figure 2B). This may be analogous to the observed low birth weight, preterm birth, and perinatal death in a developing fetus as a result of maternal smoking during pregnancy (Warren et al., 2014).

Nicotine also displayed cell-type-specific adverse effects, consistent with previous findings in animal and clinical studies (Holbrook, 2016). For example, we found that *APOE* was upregulated in nicotine-exposed EBs, and it has previously been shown that upregulated *APOE* leads to brain malformations and intellectual disability (Tanaka et al., 2018). In muscle cells, increased expression of HMGB1 impairs cardiac excitation-contraction (Zhang et al., 2014) and increases nicotine-induced risk for $Ca^{2+}$-associated arrhythmias (Figure 5). In addition, the DEGs identified by scRNA-seq analysis are similar to bulk transcriptome studies performed in human cell lines (Figure 2D).

Interestingly, we found that nicotine dysregulates the cell cycle of endothelial, stromal, and muscle progenitor cells from G1 phase to S/G2M phases. Previous studies have also shown that nicotine stimulates the cell cycle in aortic smooth muscle cells, epithelial cells, and lung cancer cells (He et al., 2014). One study shows that nicotine enhances proliferation and induces cyclin D1 to stimulate G1 to S/G2 phase transition in human bronchial smooth muscle cells (Hong et al., 2017), which is consistent with our findings in cluster-13 muscle progenitor cells. A possible mechanism is that nicotine activates RAS/MAPK pathway via nicotinic acetylcholine receptors (nAChRs) to trigger a network that positively regulates cell-cycle

progression through G1 to S, such as cyclin D (Hong et al., 2017). Here, although no expression difference was observed on cyclin D and RAS/MAPK in our scRNA-seq data, we found that the components of cell-cycle machinery, such as *HSP90AA1*, *TUBB4B*, and *TUBA1B*, which are related to G2M transition (Duggal et al., 2018), and *HNRNPH1* and *HNRNPA2B1*, which are related to G1 to S transition (Duggal et al., 2018), are upregulated in nicotine-exposed muscle cell cluster 3.

As such, scRNA-seq analysis provides a robust tool for investigating cell-to-cell interactions (Kawasaki et al., 2011; Rehan et al., 2009) in development and disease pathobiology. In particular, an activated HMGB1-TLR4 pathway was pronounced in multiple cell types within EBs upon nicotine exposure. High expression of *HMGB1* in multiple organs, perhaps induced by the secondary effects of nicotine such as oxidative stress, apoptosis, and inflammatory factors (Loukili et al., 2011; Scaffidi et al., 2002; Kim et al., 2016), and is known to mediate multiple pathological conditions (Ko et al., 2014), has been shown in smokers. For example, upregulated HMGB1 impairs cardiac excitation-contraction coupling by enhancing sarcoplasmic reticulum $Ca^{2+}$ leakage through TLR4-ROS signaling in cardiomyocytes (Zhang et al., 2014). This indicates that HMGB1 could be a potential drug target for nicotine-induced embryonic defects.

Nicotine has been suggested to mediate its function via an nAChR-dependent or -independent pathway. Nicotinic receptors are expressed in undifferentiated and differentiating cells (Figure S3C). Studies have shown that nAChRs mediate apoptosis, cell proliferation, cell differentiation, regulation of intracellular calcium, oxidative stress, and inflammation by nicotine (Dasgupta and Chellappan, 2006). In addition, nicotine is reported to promote tumor progression by binding to β-adrenergic receptors (Carlisle et al., 2007). In addition, nicotine drives both cell proliferation and cell death via paracrine signaling by cell-cell interaction (Delitto et al., 2014; Scaffidi et al., 2002). Thus, nicotine may induce the adverse effects of EBs through nAChR-dependent and -independent pathways, as well as cell-cell interaction.

Furthermore, scRNA-seq analysis can be used to optimize the treatment manner and period of drug use for patient-specific drug screening/testing. For example, with the increasing availability of commercial human genomic sequencing data, we can evaluate embryonic developmental-specific drug responses with (single nucleotide polymorphism) SNPs, and the response can be confirmed by gene editing with the CRISPR technology (Seeger et al., 2017). Specifically, the SNP (rs141819830) of the *GFI1* gene has been reported to be sensitive to maternal smoking in exposed neonates (Gonseth et al., 2016). Thus, we may be able to use patient-specific hiPSC-derived EBs carrying this SNP to evaluate the risk of nicotine toxicity on embryonic development. We anticipate that this platform should help correlate the risk of the *GFI1* SNP gene with maternal smoking during pregnancy.

In summary, we used microdroplet-based scRNA-seq to investigate the adverse effects on heterogeneous EBs upon nicotine exposure. Our study offers an effective platform to evaluate the potential effects of nicotine on human embryonic development. Our data provide potential molecular mechanisms for prenatal nicotine toxicity on specific cell populations derived from human ESCs.

## Cell Culture and Differentiation

hESC line, H7 (WiCell Research Institute), was seeded on Matrigel (BD Bioscience)-coated plates in Essential 8 Medium (Thermo Fisher Scientific). We generated EBs by clone suspension. EBs were differentiated in DMEM/F12 (Gibco) supplemented with 20% FBS (Gibco), 50 U/mL penicillin/streptomycin (Gibco), 2 mM L-glutamine (Gibco), 1× non-essential amino acids, and 100 μM β-mercaptoethanol (Sigma). At 90% confluency, hESCs were digested using 1 mL Gentle Cell Dissociation Reagent (STEMCELL Technologies) for 5 min. Cell clumps were pipetted into single cells, and $9.0 \times 10^5$ cells per well were seeded into AggreWell 800 (STEMCELL Technologies). The day after seeding, EBs/spheroids were harvested from AggreWell 800 plates and transferred into an ultra-low attachment six-well plate (Corning). Nicotine (10 μM; N3876, Sigma) was added into the differentiating medium, and EBs were fed each day for 21 days. The same volume of ethanol (459836, Sigma) was added into the differentiating medium as control.

## scRNA-Seq Library Preparation and Analysis

Single cells were collected from two independent EB differentiation experiments from day 21 EBs (control and nicotine-exposed) and dissociated using Accutase (STEMCELL Technologies). They were prepared for the single-cell library separately. In brief, cells were washed with 1× DPBS (Gibco) three times, strainer filtered, and re-suspended in 0.04% BSA. Viable single cells were loaded on to a GemCode Instrument (10× Genomics, Pleasanton, CA) to generate single-cell barcoded droplets (GEMs) using the 10× Single Cell 3′ v.2 chemistry and 10× Chromium system as per the manufacturer's protocol. The quality of the resulting libraries was checked with Bioanalyzer (Agilent Bioanalyzer 2100). Then control and nicotine libraries were combined with equal molar mass and sequenced across two lanes on an Illumina HiSeq machine. Analyses was performed using Seurat R package. Detailed scRNA-seq analysis is available in the Supplemental Experimental Procedures.

### EB Diameter Measurement

Bright-field images were captured by an SI8000 Cell Motion Imaging System (Sony Biotechnology) using a 4× objective. Scale was set with a 20-cm-ruler image. The diameter of each EB was measured by drawing a selection line of longest distance in each EB using the Line Selection tool in ImageJ. Analyses were processed with ImageJ and the results were plotted with Prism (GraphPad).

### Quantification of ROS Production and ATP

ROS production level and ATP level in EBs were determined using CellTiter-Glo 2.0 (Promega) and ROS-Glo $H_2O_2$ (Promega) following the manufacturers' instructions. In brief, EBs were exposed to nicotine in 96-well plates for 21 days. After treatment, $H_2O_2$ substrate was added directly to each well of 96-well plates and incubated for 4 h. The resulting supernatant was collected for ROS-Glo $H_2O_2$ assay and EBs were subsequently subjected to the CellTiter-Glo 2.0 assay to measure the ATP level. The luminescence intensity was measured using a Synergy HTX multi-mode microplate reader (BioTek).

### Intracellular Calcium Imaging

Single hESC-derived cardiomyocytes were plated onto Matrigel-coated coverglass (CS-24/50, Warner Instruments) at a density of ~10,000 cells per square centimeter. Cells were allowed to recover for 3–4 days and loaded with 5 μM Fura-2 AM (Thermo Fisher Scientific) in Tyrode's solution (140 mM NaCl, 5.4 mM KCl, 1 mM $MgCl_2$, 10 mM glucose, 1.8 mM $CaCl_2$, and 10 mM HEPES; pH adjusted to 7.4 with NaOH at room temperature) for 30 min at room temperature. Cells were imaged on a customized Ti-S/L 100 Inverted Microscope-based imaging platform with a 40× oil immersion objective (CFI Super Fluor, NA 1.30 WD 0.22). Bipolar pulse was used to pace cells at 0.5 and 1 HZ. Cells were kept at 37°C while recording. Fura-2 signals were captured in high-frame-rate video recording mode (512 × 512 pixels) at a speed of 50 frames per second. Videos were analyzed with NIS Elements Advanced Research Software (Nikon), and raw ratio-pair data were further processed with a custom-made script based on Interactive Digital Language.

## ACCESSION NUMBERS

The GEO accession number for single-cell RNA-seq of day 21 control and nicotine-exposed EBs in this paper is GEO: GSE125416.

## SUPPLEMENTAL INFORMATION

Supplemental Information includes Supplemental Experimental Procedures, three figures, and seven tables and can be found with this article online at https://doi.org/10.1016/j.stemcr.2019.01.022.

## AUTHOR CONTRIBUTIONS

H.G. designed the study, performed the experiment, analyzed the data, and wrote the manuscript. L.T. analyzed the scRNA-seq data and published bulk RNA-seq data, discussed the results, and wrote the manuscript. J.Z.Z. conducted $Ca^{2+}$ experiments, discussed the results, and revised the manuscript. T.K. performed the experiments, discussed the results, and revised the manuscript. D.T.P. designed the study, provided advice, and revised the manuscript. W.H.L. performed the experiments, provided advice, and revised the manuscript. J.C.W. designed the study, revised the manuscript, and provided funding support.

## ACKNOWLEDGMENTS

The authors would like to thank Dhananjay A. Wagh and John A. Coller of Stanford Functional Genomics Facility for assistance with single-cell RNA sequencing. The authors are grateful for critical reading of the manuscript by Yonggang Liu, Amanda J. Chase, and Kitchener D. Wilson. This study was funded by NIH grants T32 EB009035 (D.T.P.), TRDRP 26FT-0029 (J.Z.Z), American Heart Association Scientist Development Grant 16SDG27560003 (W.H.L), and R01 HL130020 (J.C.W.), R01 HL113006 (J.C.W.), R01 HL141371 (J.C.W.), R01 HL132875 (J.C.W.), TRDRP 27IR-0012 (J.C.W.).

Received: November 29, 2018
Revised: January 28, 2019
Accepted: January 28, 2019
Published: February 28, 2019

## REFERENCES

De Abrew, K.N., Kainkaryam, R.M., Shan, Y.Q.K., Overmann, G.J., Settivari, R.S., Wang, X.H., Xu, J., Adams, R.L., Tiesman, J.P., Carney, E.W., et al. (2016). Grouping 34 chemicals based on mode of action using connectivity mapping. Toxicol. Sci. *151*, 447–461.

Ahrens, I., Domeij, H., Topcic, D., Haviv, I., Merivirta, R.M., Agrotis, A., Leitner, E., Jowett, J.B., Bode, C., Lappas, M., et al. (2011). Successful in vitro expansion and differentiation of cord blood derived CD34+ cells into early endothelial progenitor cells reveals highly differential gene expression. PLoS One *6*, e23210.

Aiken, J., Buscaglia, G., Bates, E.A., and Moore, J.K. (2017). The alpha-tubulin gene *TUBA1A* in brain development: a key ingredient in the neuronal isotype blend. J. Dev. Biol. *5*. https://doi.org/10.3390/jdb5030008.

Armant, O., Gourain, V., Etard, C., and Strahle, U. (2016). Whole transcriptome data analysis of zebrafish mutants affecting muscle development. Data Brief *8*, 61–68.

Bao, W., Xu, G.F., Lu, J.C., Snetselaar, L.G., and Wallace, R.B. (2018). Changes in electronic cigarette use among adults in the United States, 2014–2016. JAMA *319*, 2039–2041.

Berry, F.B., Miura, Y., Mihara, K., Kaspar, P., Sakata, N., Hashimoto-Tamaoki, T., and Tamaoki, T. (2001). Positive and negative regulation of myogenic differentiation of C2C12 cells by isoforms of the multiple homeodomain zinc finger transcription factor *ATBF1*. J. Biol. Chem. *276*, 25057–25065.

Billatos, E., Faiz, A., Gesthalter, Y., LeClerc, A., Alekseyev, Y.O., Xiao, X., Liu, G., ten Hacken, N.H.T., Heijink, I.H., Timens, W., et al. (2018). Impact of acute exposure to cigarette smoke on airway gene expression. Physiol. Genomics *50*, 705–713.

Blakeley, P., Fogarty, N., Del Valle, I., Wamaitha, S., Hu, T.X., Elder, K., Snell, P., Christie, L., Robson, P., and Niakan, K. (2017). Defining the three cell lineages of the human blastocyst by single-cell RNA-seq. Mech. Dev. *145*, S26.

Carlisle, D.L., Liu, X., Hopkins, T.M., Swick, M.C., Dhir, R., and Siegfried, J.M. (2007). Nicotine activates cell-signaling pathways through muscle-type and neuronal nicotinic acetylcholine receptors in non-small cell lung cancer cells. Pulm. Pharmacol. Ther. *20*, 629–641.

Dasgupta, P., and Chellappan, S.P. (2006). Nicotine-mediated cell proliferation and angiogenesis: new twists to an old story. Cell Cycle *5*, 2324–2328.

DeLaughter, D.M., Christodoulou, D.C., Robinson, J.Y., Seidman, C.E., Baldwin, H.S., Seidman, J.G., and Barnett, J.V. (2013). Spatial transcriptional profile of the chick and mouse endocardial cushions identify novel regulators of endocardial EMT in vitro. J. Mol. Cell. Cardiol. *59*, 196–204.

Delitto, D., Han, S., Hughes, S.J., Behrns, K.E., and Trevino, J.G. (2014). Nicotine drives pancreatic cancer metastasis through paracrine signaling in the tumor microenvironment. J. Am. Coll. Surgeons *219*, E175.

Duggal, S., Jailkhani, N., Midha, M.K., Agrawal, N., Rao, K.V.S., and Kumar, A. (2018). Defining the *AKT1* interactome and its role in regulating the cell cycle. Sci. Rep. *8*, 1303.

Dumont-Lagace, M., Gerbe, H., Daouda, T., Laverdure, J.P., Brochu, S., Lemieux, S., Gagnon, E., and Perreault, C. (2017). Detection of quiescent radioresistant epithelial progenitors in the adult thymus. Front. Immunol. *8*, 1717.

Erkan, M., Kleeff, J., Esposito, I., Giese, T., Ketterer, K., Buchler, M.W., Giese, N.A., and Friess, H. (2005). Loss of *BNIP3* expression is a late event in pancreatic cancer contributing to chemoresistance and worsened prognosis. Oncogene *24*, 4421–4432.

Etard, C., Armant, O., Roostalu, U., Gourain, V., Ferg, M., and Strahle, U. (2015). Loss of function of myosin chaperones triggers HSF1-mediated transcriptional response in skeletal muscle cells. Genome Biol. *16*, 267.

Fried, P.A., and Oconnell, C.M. (1987). A comparison of the effects of prenatal exposure to tobacco, alcohol, cannabis and caffeine on birth size and subsequent growth. Neurotoxicol. Teratol. *9*, 79–85.

Geraghty, P., Wallace, A., and D'Armiento, J.M. (2011). Induction of the unfolded protein response by cigarette smoke is primarily an activating transcription factor 4-C/EBP homologous protein mediated process. Int. J. Chronic. Obstr. *6*, 309–319.

Ghosh, A., Coakley, R.C., Mascenik, T., Rowell, T.R., Davis, E.S., Rogers, K., Webster, M.J., Dang, H., Herring, L.E., Sassano, M.F., et al. (2018). Chronic e-cigarette exposure alters the human bronchial epithelial proteome. Am. J. Respir. Crit. Care Med. *198*, 67–76.

Glick, D., Zhang, W., Beaton, M., Marsboom, G., Gruber, M., Simon, M.C., Hart, J., Dorn, G.W., 2nd, Brady, M.J., Macleod, K.F., et al. (2012). *BNIP3* regulates mitochondrial function and lipid metabolism in the liver. Mol. Cell. Biol. *32*, 2570–2584.

Gonseth, S., de Smith, A.J., Roy, R., Zhou, M., Lee, S.T., Shao, X.R., Ohja, J., Wrensch, M.R., Walsh, K.M., Metayer, C., et al. (2016). Genetic contribution to variation in DNA methylation at maternal smoking-sensitive loci in exposed neonates. Epigenetics *11*, 664–673.

Gumus, Z.H., Du, B., Kacker, A., Boyle, J.O., Bocker, J.M., Mukherjee, P., Subbaramaiah, K., Dannenberg, A.J., and Weinstein, H. (2008). Effects of tobacco smoke on gene expression and cellular pathways in a cellular model of oral leukoplakia. Cancer Prev. Res. (Phila). *1*, 100–111.

He, F., Li, B., Zhao, Z., Zhou, Y., Hu, G., Zou, W., Hong, W., Zou, Y., Jiang, C., Zhao, D., et al. (2014). The pro-proliferative effects of nicotine and its underlying mechanism on rat airway smooth muscle cells. PLoS One *9*, e93508.

Hirata, N., Yamada, S., Asanagi, M., Sekino, Y., and Kanda, Y. (2016). Nicotine induces mitochondrial fission through mitofusin degradation in human multipotent embryonic carcinoma cells. Biochem. Biophys. Res. Commun. *470*, 300–305.

Holbrook, B.D. (2016). The effects of nicotine on human fetal development. Birth Defects Res. C Embryo Today *108*, 181–192.

Holownia, A., Wielgat, P., Kwolek, A., Jackowski, K., and Braszko, J.J. (2015). Crosstalk between co-cultured a549 cells and thp1 cells exposed to cigarette smoke. Adv. Exp. Med. Biol. *858*, 47–55.

Hong, W., Peng, G., Hao, B., Liao, B., Zhao, Z., Zhou, Y., Peng, F., Ye, X., Huang, L., Zheng, M., et al. (2017). Nicotine-induced airway smooth muscle cell proliferation involves TRPC6-dependent calcium influx via alpha7 nAChR. Cell Physiol. Biochem. *43*, 986–1002.

Hu, N., Han, X.F., Lane, E.K., Gao, F., Zhang, Y.M., and Ren, J. (2013). Cardiac-specific overexpression of metallothionein rescues against cigarette smoking exposure-induced myocardial contractile and mitochondrial damage. PLoS One *8*, e57151.

Jaddoe, V.W.V., Troe, E.J.W.M., Hofman, A., Mackenbach, J.P., Moll, H.A., Steegers, E.A.P., and Witteman, J.C.M. (2008). Active and passive maternal smoking during pregnancy and the risks of low birthweight and preterm birth: the Generation R Study. Paediatr. Perinat. Epidemiol. *22*, 162–171.

Kawasaki, H., Takatori, S., Zamami, Y., Koyama, T., Goda, M., Hirai, K., Tangsucharit, P., Jin, X., Hobara, N., and Kitamura, Y. (2011). Paracrine control of mesenteric perivascular axo-axonal interaction. Acta Physiol. (Oxf.) *203*, 3–11.

Kim, C.S., Choi, J.S., Joo, S.Y., Bae, E.H., Ma, S.K., Lee, J., and Kim, S.W. (2016). Nicotine-induced apoptosis in human renal proximal tubular epithelial cells. PLoS One *11*, e0152591.

Kimura, A., Matsuda, T., Sakai, A., Murao, N., and Nakashima, K. (2018). *HMGB2* expression is associated with transition from a quiescent to an activated state of adult neural stem cells. Dev. Dyn. *247*, 229–238.

Ko, Y.B., Kim, B.R., Nam, S.L., Yang, J.B., Park, S.Y., and Rho, S.B. (2014). High-mobility group box 1 (HMGB1) protein regulates tumor-associated cell migration through the interaction with BTB domain. Cell. Signal. *26*, 777–783.

Larsen, H.E., Lefkimmiatis, K., and Paterson, D.J. (2016). Sympathetic neurons are a powerful driver of myocyte function in cardiovascular disease. Sci. Rep. *6*, 38898.

Lin, C., Yon, J.M., Hong, J.T., Lee, J.K., Jeong, J., Baek, I.J., Lee, B.J., Yun, Y.W., and Nam, S.Y. (2014). 4-O-Methylhonokiol inhibits serious embryo anomalies caused by nicotine via modulations of oxidative stress, apoptosis, and inflammation. Birth Defects Res. B Dev. Reprod. Toxicol. *101*, 125–134.

Liszewski, W., Ritner, C., Aurigui, J., Wong, S.S.Y., Hussain, N., Krueger, W., Oncken, C., and Bernstein, H.S. (2012). Developmental effects of tobacco smoke exposure during human embryonic stem cell differentiation are mediated through the transforming growth factor-beta superfamily member, nodal. Differentiation *83*, 169–178.

Liu, W.W., Jin, G.R., Long, C.D., Zhou, X., Tang, Y., Huang, S., Kuang, X.L., Wu, L.Z., Zhang, Q.J., and Shen, H.X. (2013). Blockage of notch signaling inhibits the migration and proliferation of retinal pigment epithelial cells. ScientificWorldJournal *2013*, 178708.

Liu, X., Wang, C.N., Qiu, C.Y., Song, W., Wang, L.F., and Liu, B. (2017). Adipocytes promote nicotine-induced injury of endothelial cells via the NF-κB pathway. Exp. Cell Res. *359*, 251–256.

Loinard, C., Zouggari, Y., Rueda, P., Ramkhelawon, B., Cochain, C., Vilar, J., Recalde, A., Richart, A., Charue, D., Duriez, M., et al. (2012). C/EBP homologous protein-10 (CHOP-10) limits postnatal neovascularization through control of endothelial nitric oxide synthase gene expression. Circulation *125*, 1014–U1126.

Loukili, N., Rosenblatt-Velin, N., Li, J., Clerc, S., Pacher, P., Feihl, F., Waeber, B., and Liaudet, L. (2011). Peroxynitrite induces HMGB1 release by cardiac cells in vitro and HMGB1 upregulation in the infarcted myocardium in vivo. Cardiovasc. Res. *89*, 586–594.

Luck, W., Nau, H., Hansen, R., and Steldinger, R. (1985). Extent of nicotine and cotinine transfer to the human-fetus, placenta and amniotic-fluid of smoking mothers. Dev. Pharmacol. Ther. *8*, 384–395.

Malmstrom, J., Lindberg, H., Lindberg, C., Bratt, C., Wieslander, E., Delander, E.L., Sarnstrand, B., Burns, J.S., Mose-Larsen, P., Fey, S., et al. (2004). Transforming growth factor-beta(1) specifically induce proteins involved in the myofibroblast contractile apparatus. Mol. Cell. Proteomics *3*, 466–477.

Martynova, N.Y., Eroshkin, F.M., Orlov, E.E., and Zaraisky, A.G. (2018). HMG-Box factor SOXD/SOX15 and homeodomain-containing factor XANF1/HESX1 directly interact and regulate the expression of XANF1/HESX1 during early forebrain development in *Xenopus laevis*. Gene *638*, 52–59.

Matsuura, K., Otani, M., Takano, M., Kadoyama, K., and Matsuyama, S. (2016). The influence of chronic nicotine treatment on proteins expressed in the mouse hippocampus and cortex. Eur. J. Pharmacol. *780*, 16–25.

de Melo, J., Zibetti, C., Clark, B.S., Hwang, W., Miranda-Angulo, A.L., Qian, J., and Blackshaw, S. (2016). *LHX2* is an essential factor for retinal gliogenesis and notch signaling. J. Neurosci. *36*, 2391–2405.

Michelotti, G.A., Tucker, A., Machado, M.V., Swiderska-Syn, M., Choi, S.S., Kruger, L., Garman, K.S., Moylan, C.A., Guy, C.D., Himburg, H., et al. (2014). Pleiotrophin regulates the ductular reaction by controlling the migration of cells in liver progenitor niches. Hepatology *60*, 408a.

Mohsenzadeh, Y., Rahmani, A., Cheraghi, J., Pyrani, M., and Asadollahi, K. (2014). Prenatal exposure to nicotine in pregnant rat increased inflammatory marker in newborn rat. Mediat. Inflamm. *2014*, 274048.

Moreno-Gonzalez, I., Estrada, L.D., Sanchez-Mejias, E., and Soto, C. (2013). Smoking exacerbates amyloid pathology in a mouse model of Alzheimer's disease. Nat. Commun. *4*, 1495.

Nestorowa, S., Hamey, F.K., Pijuan Sala, B., Diamanti, E., Shepherd, M., Laurenti, E., Wilson, N.K., Kent, D.G., and Gottgens, B. (2016). A single-cell resolution map of mouse hematopoietic stem and progenitor cell differentiation. Blood *128*, e20–31.

Paik, D.T., Tian, L., Lee, J., Sayed, N., Chen, I.Y., Rhee, S., Rhee, J.W., Kim, Y., Wirka, R.C., Buikema, J.W., et al. (2018). Large-scale single-cell RNA-seq reveals molecular signatures of heterogeneous populations of human induced pluripotent stem cell-derived endothelial cells. Circ. Res. *123*, 443–450.

Pei, F., Jiang, J.J., Bai, S.Y., Cao, H.H., Tian, L.Y., Zhao, Y., Yang, C.X., Dong, H.H., and Ma, Y. (2017). Chemical-defined and albumin-free generation of human atrial and ventricular myocytes from human pluripotent stem cells. Stem Cell Res. *19*, 94–103.

Popson, S.A., Ziegler, M.E., Chen, X.F., Holderfield, M.T., Shaaban, C.I., Fong, A.H., Welch-Reardon, K.M., Papkoff, J., and Hughes, C.C.W. (2014). Interferon-induced transmembrane protein 1 regulates endothelial lumen formation during angiogenesis. Arterioscler. Thromb. Vasc. Biol. *34*, 1011–1019.

Ramilowski, J.A., Goldberg, T., Harshbarger, J., Kloppman, E., Lizio, M., Satagopam, V.P., Itoh, M., Kawaji, H., Carninci, P., Rost, B., et al. (2015). A draft network of ligand-receptor-mediated multicellular signalling in human. Nat. Commun. *6*, 7866.

Rehan, V.K., Asotra, K., and Torday, J.S. (2009). The effects of smoking on the developing lung: insights from a biologic model for lung development, homeostasis, and repair. Lung *187*, 281–289.

Repo, J.K., Pesonen, M., Mannelli, C., Vahakangas, K., and Loikkanen, J. (2014). Exposure to ethanol and nicotine induces stress responses in human placental BeWo cells. Toxicol. Lett. *224*, 264–271.

Saito, T., Yano, F., Mori, D., Ohba, S., Hojo, H., Otsu, M., Eto, K., Nakauchi, H., Tanaka, S., Chung, U., et al. (2013). Generation of COL2A1-EGFP iPS cells for monitoring chondrogenic differentiation. PLoS One *8*, e74137.

Satija, R., Farrell, J.A., Gennert, D., Schier, A.F., and Regev, A. (2015). Spatial reconstruction of single-cell gene expression data. Nat. Biotechnol. *33*, 495–502.

Sauler, M., Bucala, R., and Lee, P.J. (2015). Role of macrophage migration inhibitory factor in age-related lung disease. Am. J. Physiol. Lung Cell Mol. Physiol. *309*, L1–L10.

Scaffidi, P., Misteli, T., and Bianchi, M.E. (2002). Release of chromatin protein HMGB1 by necrotic cells triggers inflammation. Nature *418*, 191–195.

Seeger, T., Porteus, M., and Wu, J.C. (2017). Genome editing in cardiovascular biology. Circ. Res. *120*, 778–780.

Shen, Y.P., Zhang, F., Lan, H.R., Chen, K., Zhang, Q., Xie, G.M., Teng, L.S., and Jin, K.T. (2015). Frzb up-regulation is correlated with hepatic metastasis and poor prognosis in colon carcinoma patients with hepatic metastasis. Int. J. Clin. Exp. Pathol. *8*, 4083–4090.

Sheng, X.M., and Wang, Z.X. (2016). Protein arginine methyltransferase 5 regulates multiple signaling pathways to promote lung cancer cell proliferation. BMC Cancer *16*, 567.

Slotkin, T.A. (1998). Fetal nicotine or cocaine exposure: which one is worse? J. Pharmacol. Exp. Ther. *285*, 931–945.

Slotkin, T.A., Cho, H., and Whitmore, W.L. (1987). Effects of prenatal nicotine exposure on neuronal development - selective actions on central and peripheral catecholaminergic pathways. Brain Res. Bull. *18*, 601–611.

Sugrue, S.P., Akin, D., Newman, J., and McIntyre, L. (2016). RNA-seq analysis of impact of PNN on gene expression and alternative splicing in corneal epithelial cells. Invest. Ophth. Vis. Sci. *57*, 4369.

Tabib, T., Morse, C., Wang, T., Chen, W., and Lafyatis, R. (2018). SFRP2/DPP4 and FMO1/LSP1 define major fibroblast populations in human skin. J. Invest. Dermatol. *138*, 802–810.

Tanaka, H., Kondo, K., Chen, X., Homma, H., Tagawa, K., Kerever, A., Aoki, S., Saito, T., Saido, T., Muramatsu, S.I., et al. (2018). The intellectual disability gene PQBP1 rescues Alzheimer's disease pathology. Mol. Psychiatry *23*, 2090–2110.

Tang, H., Liu, Y.J., Liu, M., and Li, X. (2007). Establishment and gene analysis of an oxaliplatin-resistant colon cancer cell line thc8307/l-ohp. Anticancer Drugs *18*, 633–639.

Tang, K., Xie, X., Park, J.I., Jamrich, M., Tsai, S., and Tsai, M.J. (2010). COUF-TFS regulate eye development by controlling factors essential for optic vesicle morphogenesis. Development *137*, 725–734.

Tchetchelnitski, V., van den Eijnden, M., Schmidt, F., and Stoker, A.W. (2014). Developmental co-expression and functional redundancy of tyrosine phosphatases with neurotrophin receptors in developing sensory neurons. Int. J. Dev. Neurosci. *34*, 48–59.

Tizabi, Y. (2007). Nicotine and nicotinic system in hypoglutamatergic models of schizophrenia. Neurotox. Res. *12*, 233–246.

Warren, G.W., Alberg, A.J., Kraft, A.S., and Cummings, K.M. (2014). The 2014 Surgeon General's report: "The health consequences of smoking–50 years of progress": a paradigm shift in cancer care. Cancer *120*, 1914–1916.

Winzer-Serhan, U.H. (2008). Long-term consequences of maternal smoking and developmental chronic nicotine exposure. Front. Biosci. *13*, 636–649.

Wong, M.K., Holloway, A.C., and Hardy, D.B. (2016). Nicotine directly induces endoplasmic reticulum stress response in rat placental trophoblast giant cells. Toxicol. Sci. *151*, 23–34.

Xu, R.H., Liu, B., Wu, J.D., Yan, Y.Y., and Wang, J.N. (2016). Mir-143 is involved in endothelial cell dysfunction through suppression of glycolysis and correlated with atherosclerotic plaques formation. Eur. Rev. Med. Pharmacol. *20*, 4063–4071.

Yazdani, N., Parker, C.C., Shen, Y., Reed, E.R., Guido, M.A., Kole, L.A., Kirkpatrick, S.L., Lim, J.E., Sokoloff, G., Cheng, R.Y., et al. (2015). HNRNPH1 is a quantitative trait gene for methamphetamine sensitivity. Plos Genet. *11*, e1005713.

Yoshiyama, S., Chen, Z.Y., Okagaki, T., Kohama, K., Nasu-Kawaharada, R., Izumi, T., Ohshima, N., Nagai, T., and Nakamura, A. (2014). Nicotine exposure alters human vascular smooth muscle cell phenotype from a contractile to a synthetic type. Atherosclerosis *237*, 464–470.

Zdravkovic, T., Genbacev, O., LaRocque, N., McMaster, M., and Fisher, S. (2008). Human embryonic stem cells as a model system for studying the effects of smoke exposure on the embryo. Reprod. Toxicol. *26*, 86–93.

Zhang, C.C., Mo, M.H., Ding, W.W., Liu, W.J., Yan, D.W., Deng, J.X., Luo, X.P., and Liu, J. (2014). High-mobility group box 1 (HMGB1) impaired cardiac excitation-contraction coupling by enhancing the sarcoplasmic reticulum (SR) $Ca_{2+}$ leak through TLR4-ROS signaling in cardiomyocytes. J. Mol. Cell. Cardiol. *74*, 260–273.

Zhao, Y.U., Sheng, H.Z., Amini, R., Grinberg, A., Lee, E., Huang, S.P., Taira, M., and Westphal, H. (1999). Control of hippocampal morphogenesis and neuronal differentiation by the LIM homeobox gene lhx5. Science *284*, 1155–1158.

Zhu, Z.R., Li, Q.V., Lee, K., Rosen, B.P., Gonzalez, F., Soh, C.L., and Huangfu, D.W. (2016). Genome editing of lineage determinants in human pluripotent stem cells reveals mechanisms of pancreatic development and diabetes. Cell Stem Cell *18*, 755–768.

**Stem Cell Reports, Volume *12***

## Supplemental Information

# Single-Cell RNA Sequencing of Human Embryonic Stem Cell Differentiation Delineates Adverse Effects of Nicotine on Embryonic Development

**Hongchao Guo, Lei Tian, Joe Z. Zhang, Tomoya Kitani, David T. Paik, Won Hee Lee, and Joseph C. Wu**

# Supplemental Information

## Single-Cell RNA-Sequencing of Human Embryonic Stem Cell Differentiation Delineates Adverse Effects of Nicotine on Embryonic Development

Hongchao Guo[1,2,3,*], Lei Tian[1,2,3,*], Joe Z. Zhang[1,2,3], Tomoya Kitani[1,2,3], David T. Paik[1,2,3], Won Hee Lee[4], Joseph C. Wu[1,2,3]

[1]Stanford Cardiovascular Institute, Stanford, CA 94305, USA; [2]Institute for Stem Cell Biology and Regenerative Medicine, Stanford, CA 94305, USA; [3]Division of Cardiology, Department of Medicine, Stanford University School of Medicine, Stanford, CA 94305, USA; [4]Department of Basic Medical Sciences, University of Arizona College of Medicine, Phoenix, AZ 85004, USA

[*]Co-first author

## Supplemental Methods

**Reads mapping.** FastQ files containing sequenced reads were mapped to the human reference genome (GRCh38) following "One Library, Multiple Flowcells" pipeline with Cellranger (version 2.1.1). Briefly, Cellranger firstly used STAR software to align sequenced reads to the reference genome. Then mapped reads were assigned to intergenic, intronic, and exonic regions based on the GTF annotation. A read was exonic if more than half of it intersects with an exon. Next, for reads that are not only aligned to a single exonic locus but also to 1 or more non-exonic loci, the exonic locus was prioritized and the read was considered to be confidently mapped to the exonic locus with a mapping quality score 255. Only reads that were confidently mapped to the transcriptome were used for UMI counting. Finally, we detected 6,847 and 5,646 cells for control and nicotine EBs, respectively. More details of mapping statistics were shown in **Table S1**.

**Bioinformatics analysis.** Cells with fewer than 200 or more than 6,000 expressed genes, and a high percentage of mitochondrial genes (>20%) were removed. Among them, 6,766 and 5,514 cells passed the filtering. We next normalized the gene expression values for each cell by the total expression, multiplied by 10,000, and made a log-transformation. Variable expressed genes across the single cells under cutoff with an average expression of more than 0.0125 and less than 3, and dispersion of more than 0.5, were detected for down-stream analysis. For dimensionality reduction and clustering, we used scaled z-scored residuals after regressing out mitochondrial percentage and the number of UMIs. Principal Component Analysis (PCA) was performed using variable expressed genes, and top 20 principal components (PCs) were used for cell clustering with a graph-based clustering approach at resolution 0.8. We ran t-SNE with the same number of PCs and default parameters to visualize the clustering results. Differentially expressed genes for each

cluster were detected by comparing cells within the cluster with other cells using the Wilcoxon rank sum test under cutoff with a *P* value less than 1%, log fold-change more than 0.25, and more than 25% cells expressing the gene. Cell cycle phase score for each cell was calculated based on the expression of G2M and S phase markers obtained from previous publication (Nestorowa et al., 2016). All these steps were performed using Seurat R package (Butler et al., 2018). We only detected the positive markers for each cluster. Functional enrichment analyses of differentially expressed genes were performed using the Bioconductor package "GeneAnswers" (Feng et al., 2018) in R (R Core Team, 2017). Functional annotations were from Gene Ontology (GO) (GO.db, Ashburner et al., 2000) and Reactome Pathway ( Reactome.db, Fabregat et al., 2018) databases. Chord plots were generated with GOplot R package (Walter et al., 2015).

Merged data with combined raw data matrix from control and nicotine-exposed embryoid bodies (EBs) were used for integrative analysis. Steps for quality control, data normalization and transformation, dimensionality reduction, and clustering were the same as described above. Within each cluster, we detected differentially expressed genes (DEGs) between control and nicotine-exposed EBs with *P* value less than 1%, log fold-change more than log(1.2), and more than 10% cells expressing the gene. Gene expressions from published datasets were directly downloaded from GEO databases with GEO accession numbers GSE69844 (hepatic cell line, HepaRG) (De Abrew et al., 2016), GSE89923 (human gingival epithelium cell line, HGEC) (Gumus et al., 2008), and GSE56383 (human smooth muscle cell, HSMC) (Yoshiyama et al., 2014). We also included an unpublished dataset that contains human iPSC-derived endothelial cells (hiPSC-ECs) with nicotine exposure and controls. Fold-changes of DEGs between nicotine-exposed and control EBs for each dataset were calculated for comparison.

**Cell-cell communications.** We downloaded human ligand-receptor pairs curated by Ramilowski et al. (Ramilowski et al., 2016). Ligands/receptors expressing in a cluster were defined if more than 25% cells in that cluster had an expression value larger than 0. The ribbons connecting cell clusters were colored according to the cluster broadcasting the ligand and connected to the cluster expressing the receptor. The size of a ribbon is proportional to the number of ligand-receptor pairs, thus demonstrating the activity of the communications. We used the igraph R package for visualization (Csardi and Nepusz, 2006).

**Differentiation of hESCs to cardiomyocytes.** For cardiac differentiation, a chemically defined monolayer differentiation protocol was used as previously described (Burridge et al., 2014). Briefly, hESCs at ~90% confluence were incubated with a differentiation basal medium comprising RPMI 1640 medium (GIBCO) and B27 supplement minus insulin (GIBCO). CHIR99021 (Selleck Chemicals), a selective glycogen synthase kinase 3β inhibitor, was added to the differentiation basal medium. On day 2, the medium was removed and replaced with differentiation basal medium minus CHIR99021. On day 3, the Wnt antagonist, IWR-1 (Selleck Chemicals), was added to the medium. After 48 hours, the medium was removed and replaced with the differentiation basal medium without any inhibitors. On day 7, the cells were incubated with the complete cardiomyocyte medium consisting of RPMI 1640 medium and B27 supplement plus insulin (GIBCO). The medium was changed every 2 days. Monolayers of hESC-derived cardiomyocytes were cultured for ~30 days and subsequently dissociated for experimental use with TrypLE Express (GIBCO). One μM nicotine was added during the cardiomyocyte differentiation process.

**Immunofluorescence and confocal microscopy.** hESC-derived cardiomyocytes were fixed in 4% paraformaldehyde in PBS. Following permeabilization with 0.3% Triton X-100, hESC-derived cardiomyocytes were stained with primary antibodies against cardiac troponin T type 2 (TNNT2; ab45932, Abcam) and alpha Actinin antibody (ACTN; ab68167, Abcam). After reaction with the primary antibodies, cells were incubated with the appropriate Alexa Fluor-conjugated secondary antibodies (Santa Cruz Biotechnology or Life Technologies). Images of the stained cells were obtained under a brightfield microscope (Leica). Confocal images were taken by using a 63 × Plan-Apochromat oil immersion objective (Carl Zeiss) and a LSM 510 Meta confocal microscope (Carl Zeiss). Images were analyzed by using ZEN software (Carl Zeiss) and ImageJ software (National Institutes of Health).

**Quantitative RT-PCR.** Total RNA was isolated using Direct-zol™ RNA MiniPrep (Zymo Research) following the manufacturer's instructions. For the reverse transcription, iScript™ cDNA Synthesis Kit (Bio-Rad) was used, and cDNA template was synthesized based on 0.5 μg of total RNA. After diluting 10 times of cDNA, 2 μL of the cDNA template, 0.5 μL of TaqMan® primer sets (Life Technology), 5 μL of TaqMan® Master Mix (Life Technology), and 2.5 μL ddH2O were mixed in the reaction system. Real-time quantitative PCR was performed with CFX Connect™ Real-Time PCR Detection System (Bio-Rad). Each reaction was run in replicates to minimize variation. Expression values were normalized to the average expression of GAPDH. Taqman assay IDs for GAPDH, HMGB1, and TLR4 are Hs02758991_g1, Hs01590761_g1, and Hs00152939_m1, respectively.

**Western blot**. Cultured cells were homogenized in RIPA buffer with proteinase inhibitors and

quantified by Pierce™ BCA Protein Assay Kit (Pierce Biotechnology Inc.). A total of 20 μg protein was separated by NuPAGE® Novex® 4-12% Bis-Tris Protein Gel (Invitrogen, Carlsbad, CA). After transfer to an Amersham™ Hybond™ Blotting Membranes (GE Healthcare), the protein lanes were analyzed by western blot using specific antibodies against GAPDH (MA5-15738-HRP, Thermo Fisher Scientific) and BNIP3 (ab10433, Abcam). Band intensity was analyzed and quantified by ImageJ Fuji program.

**Quantification and statistical analysis.** Statistical analyses for each experiment are described in the figure legends or in the appropriate text. Multiple group comparisons were calculated using one-way ANOVA. Pairwise comparisons were carried out using the two-tailed unpaired Student's t test. $*P < 0.05$; $**P < 0.01$; $***P < 0.005$; $**** P < 0.001$. All error bars are defined as standard error mean of the mean (SEM) unless otherwise indicated.

**Supplemental References**


Ashburner, M., Ball, C.A., Blake, J.A., Botstein, D., Butler, H., Cherry, J.M., Davis, A.P., Dolinski, K., Dwight, S.S., Eppig, J.T., et al. (2000). Gene ontology: Tool for the unification of biology. Nat. Genet. *25*, 25–29.

Butler, A., Hoffman, P., Smibert, P., Papalexi, E., and Satija, R. (2018). Integrating single-cell transcriptomic data across different conditions, technologies, and species. Nat. Biotechnol. *36*, 411.

Csardi, G., and Nepusz, T. (2006). The igraph software package for complex network research. InterJournal, Complex Systems 1695 (5): 1--9 (2006).

De Abrew, K.N., Kainkaryam, R.M., Shan, Y.Q.K., Overmann, G.J., Settivari, R.S., Wang, X.H., Xu, J., Adams, R.L., Tiesman, J.P., Carney, E.W., et al. (2016). Grouping 34 chemicals based on mode of action using connectivity mapping. Toxicol Sci 151, 447-461.

Fabregat, A., Jupe, S., Matthews, L., Sidiropoulos, K., Gillespie, M., Garapati, P., Haw, R., Jassal, B., Korninger, F., May, B., et al. (2018). The reactome pathway knowledgebase. *46*, 649–655.

Feng, G., Du, P., Kibbe, W.A., and Lin, S. (2018). GeneAnswers, integrated interpretation of genes overview of GeneAnswers installation of GeneAnswers package. *2*.

Gumus, Z.H., Du, B., Kacker, A., Boyle, J.O., Bocker, J.M., Mukherjee, P., Subbaramaiah, K., Dannenberg, A.J., and Weinstein, H. (2008). Effects of tobacco smoke on gene expression and cellular pathways in a cellular model of oral leukoplakia. Cancer Prev Res 1, 100-111.

Nestorowa, S., Hamey, F.K., Pijuan Sala, B., Diamanti, E., Shepherd, M., Laurenti, E., Wilson, N.K., Kent, D.G., and Göttgens, B. (2016). A single-cell resolution map of mouse hematopoietic stem and progenitor cell differentiation. Blood *128*, e20–e31.

Burridge, P.W., Matsa, E., Shukla, P., Lin, Z.C., Churko, J.M., Ebert, A.D., Lan, F., Diecke, S., Huber, B., Mordwinkin, N.M., et al. (2014). Chemically defined generation of human cardiomyocytes. Nat Methods 11, 855-860.

R Core Team (2018). R: A language and environment for statistical computing. R foundation for statistical computing, Vienna, Austria. Available online at https://www.R-project.org/.

Ramilowski, J.A., Goldberg, T., Harshbarger, J., Kloppmann, E., Lizio, M., Satagopam, V.P., Itoh, M., Kawaji, H., Carninci, P., Rost, B., et al. (2016). A draft network of ligand–receptor-mediated multicellular signalling in human. Nature Communications volume 6, Article number: 7866 (2015)

Walter, W., Sánchez-Cabo, F., and Ricote, M. (2015). GOplot: An R package for visually combining expression data with functional analysis. Bioinformatics *31*, 2912–29

Yoshiyama, S., Chen, Z.Y., Okagaki, T., Kohama, K., Nasu-Kawaharada, R., Izumi, T., Ohshima, N., Nagai, T., and Nakamura, A. (2014). Nicotine exposure alters human vascular smooth muscle cell phenotype from a contractile to a synthetic type. Atherosclerosis 237, 464-470.

**Supplemental Figure Legends**

**Figure S1. Quality control of data set and cell type identification in control and nicotine-exposed embryoid bodies (EBs). (A)** Scatter diagram showing the gene numbers (nGene) (left) and transcript numbers of single cells (nUMI) (right). **(B)** t-SNE plots of single cells from control and nicotine-exposed EBs at day 21. We identified six main types of progenitor cells in both control (top) and nicotine-exposed (bottom) EBs, including neural progenitor cells (Clusters 4, 6, and 8 in control EBs; Clusters 3, 5, 8, and 11 in nicotine-exposed EBs), stromal progenitor cells (Cluster 3 in control EBs; Cluster 6 in nicotine-exposed EBs), endothelial progenitor cells (Cluster 10 in control EBs; Cluster 10 in nicotine-exposed EBs), epithelial progenitor cells (Cluster 2 in control EBs; Cluster 2 in nicotine-exposedEBs), muscle progenitor cells (Clusters 5 and 11 in control EBs; Clusters 7 and 12 in nicotine-exposed EBs), and liver progenitor cells (Cluster 7 in control EBs; Cluster 4 in nicotine-exposed EBs). In addition, undifferentiated stem-like cells (USCs, Cluster 1) and undetermined cells (UDCs, Cluster 9) were also identified. **(C)** Heatmaps showing the expression pattern of the top 10 differentiated genes in each progenitor cell type in control (top) and nicotine-exposed (bottom) EBs. Representative differential genes for each cell type in control and nicotine-exposed EBs are listed on the right. The full list of differential genes for each cluster in control and nicotine-exposed EBs is shown in **Table S2**. **(D)** Significant gene markers for each cluster in combined EBs were selected to perform GO analysis. GO terms with $P < 0.05$ are shown. Gene number of each GO term is listed on the left. *P* value is shown as –log 10 (*P value*). Neural, muscle (Clusters 7 and 13), and epithelial (Clusters 2 and 12) progenitor cells consisted of several sub-clusters. EpiPCs were divided into two subsets: Clusters 2 and 12. Neural progenitor cells were divided into four subsets: Clusters 3, 4, 8, and 10. Muscle progenitor cells were divided into two subsets: Clusters 7 and 13. The full list of differential genes for each cluster

in combined EBs is shown in **Table S3** and differential genes-related GO terms for each cluster is shown in **Table S4**.

**Figure S2. Cell type proportions and GO analysis for each individual in combined EBs. (A)** Percentage of total cells in control and nicotine-exposed EBs is determined for each cluster. C, control EBs; N, nicotine-exposed EBs. **(B)** Proportion of cells in G2M, S, or G1 phase for each cell type. **(C)** Enriched differentially expressed genes (DEGs) related to pathways in each cell type upon nicotine exposure. The ribbons connect each gene to the assigned pathways. The color of a ribbon is consistent with the color at the pathway side to distinguish pathways. The gradient of red/blue is proportional to the fold-change of genes connected between the nicotine and control. The full list of DEGs is shown in **Table S5** and the list of DEG-related GO terms is shown in **Table S6**. **(D)** Nicotine reduced BNIP3 protein level. Upper: Representative western blot of BINP3 protein expression in control and nicotine-exposed EBs; Lower: Quantification of BINP3 expression from three independent experimetns, normalized to GAPDH. $^{**}P < 0.01$. **(E)** Genes that have consistent changes on RNA and protein expression level between found in available nicotine-associated proteomic dataset in PubMed and our scRNA-seq. **(F)** t-SNE plots of nicotine receptors, *CHRNA5*, and *CHRNB1*. Each cell on the t-SNE plot is colored according to gene expression. Gray: cells with no expression. Blue: cells with expression.

**Figure S3. Generation and characterization hESC-derived cardiomyocytes. (A)** Schematic for differentiation of hESC-derived cardiomyocytes (-insulin: B27 and RPMI without insulin, with glucose; + Insulin: B27 and RPMI with insulin and glucose; -Glucose: B27 and RPMI without insulin without Glucose). Scale bar, 100 μm. **(B)** Immunofluorescence analyses showing hESC-

derived cardiomyocytes expressing TNNT2 (green) and ACTN1 (red). Scale bar, 20 μm. **(C)** Representative FACS analysis of TNNT2 expression in hESC-derived cardiomyocytes with TNNT2 antibody (upper) and rabbit IgG antibody (lower). Statistical analysis data from C. (**$P < 0.01$; unpaired Student's t-test; and n = 3). **(D)** Cell viability assay based on quantitation of the ATP present in control and nicotine-exposed hESCs. Cell viability were measured from three independent experiments. * $P<0.05$.

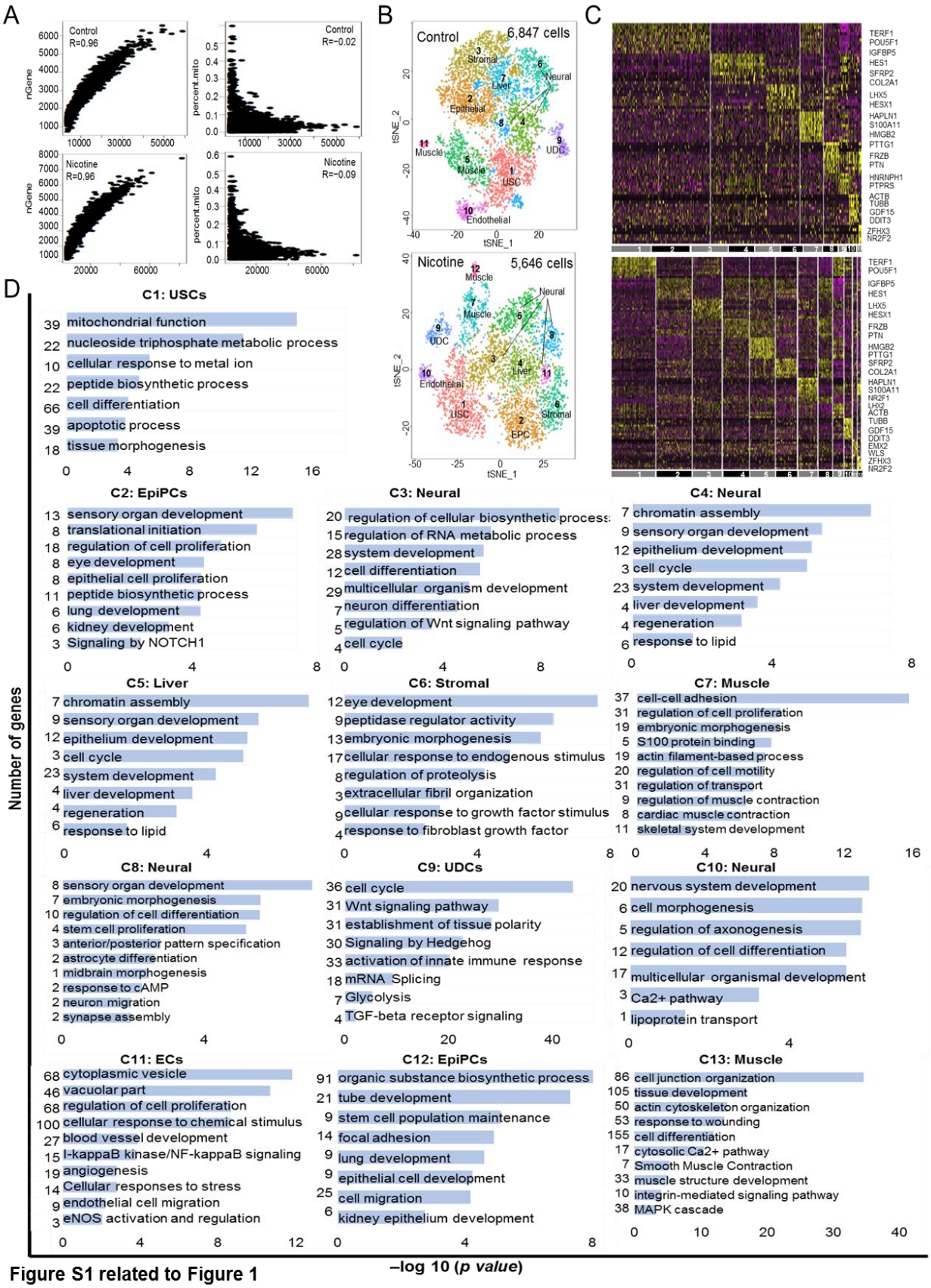


**Figure S1 related to Figure 1**

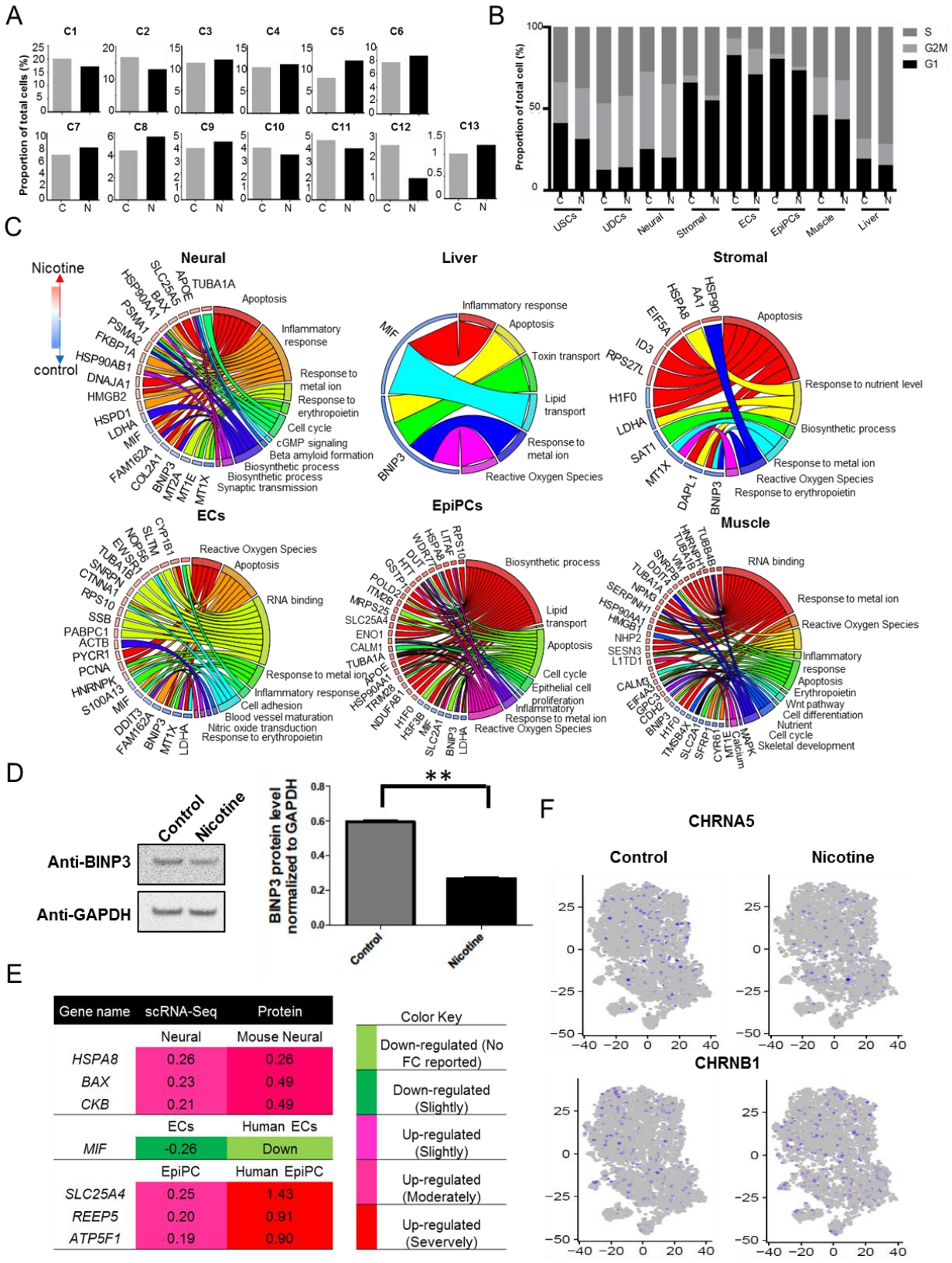


**Figure S2 related to Figure 2**

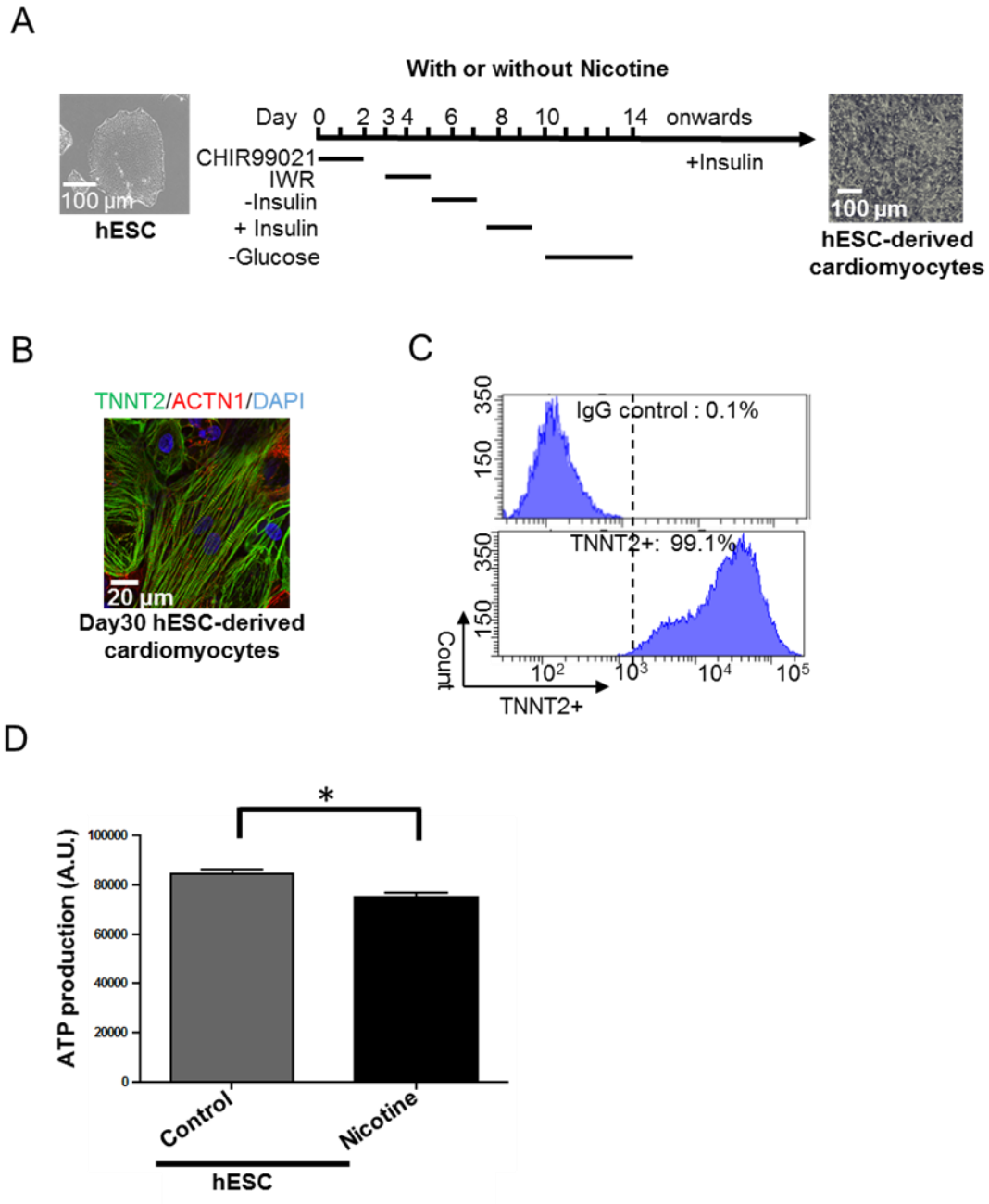


**Figure S3 related to Figure 5**

## Supplemental Tables

**Table S1. Mapping statistics, related to Figure 1.**

| Sample | Estimated number of cells | Mean reads per cell | Mean genes per cell | Read mapped confidently to genome | Read mapped confidently to transcriptome |
|---|---|---|---|---|---|
| Control EBs | 6,847 | 35,989 | 2,495 | 95.3% | 70.7% |
| Nicotine EBs | 5,646 | 54,034 | 2,896 | 93.3% | 72.3% |

**Table S2. Statistics for differentially expressed genes among clusters in control and nicotine-exposed EBs, related to Figure 1.** "pct.1" is the proportion of cells that express the gene in the target cluster, as labeled in the "cluster" column. "pct.2" is the proportion of cells that express the gene in the other clusters. (Differentially expressed genes for control and nicotine EB.xlsx).

**Table S3. Statistics for differentially expressed genes among clusters in the combined EBs, related to Figure 1.** The format is the same as Table S2. (Differentially expressed genes for combined EBs.xlsx).

**Table S4. Pathway enrichment of differentially expressed genes among clusters in the combined EBs, related to Figure 1.** The format is the same as Table S3. (Pathway Enrichment for combined EBs.xlsx).

**Table S5. Statistics for differentially expressed genes between nicotine-exposed and control EBs in each cluster, related to Figure 2.** "pct.1" is the proportion of cells that express the gene in the target cluster, which is labeled in the "cluster" column, where "D" is control and "N" is

nicotine-exposed. “pct.2” is the proportion of cells that express the gene in the other clusters. (Nicotine.vs.Control.DEGs.xlsx).

**Table S6. Pathway enrichment of differentially expressed genes between nicotine-exposed and control EBs in each cell type, related to Figure 2.** The *P*-value was calculated under the hypergeometric test. nGenes is the number of DEGs involved in the pathway. Z-score was calculated using the following formula: z-score=(up-down)/$\sqrt{}$(up+down), where up/down is the number of genes up-regulated/down-regulated in the nicotine cells. (Nicotine.vs.Control.PathwayEnrichment.xlsx).

**Table S7. Cross-talk among cell types in control and nicotine-exposed EBs, related to Figure 4.** “Ligand Clusters” column lists the cell types with more than 25% cells expressing the ligand. “Receptor Clusters” column lists the cell types with more than 25% cells expressing the receptor. (Control and nicotine EBs.crossTalks.xlsx).